Hexaisopropoxyditungsten and Dodecaisopropoxytetratungsten: $W_2(O\text{-}i\text{-}Pr)_6$ and $W_4(O\text{-}i\text{-}Pr)_{12}$. 1. Preparation, Structure, and Bonding. The First Example of a Metal-Metal Triple Bond and Its 12-Electron Cluster. Analogies with Ethyne and Cyclobutadiene

Malcolm H. Chisholm,* David L. Clark, Kirsten Folting, John C. Huffman, and Mark Hampden-Smith

Contribution from the Department of Chemistry and Molecular Structure Center, Indiana University, Bloomington, Indiana 47405. *Received March 30, 1987*

Abstract: The reaction between $W_2(O\text{-}t\text{-}Bu)_6$ and *i*-PrOH (>6 equiv) in dme (dme = 1,2-dimethoxyethane) yields a black crystalline product, which has been shown to be a 1:1 mixture of $W_4(O\text{-}i\text{-}Pr)_{12}$ and $W_2(O\text{-}i\text{-}Pr)_6$ by an X-ray study. Crystal data at −156 °C: a = 12.277 (3), b = 12.890 (3), c = 12.118 (3) Å; α = 94.60 (1), β = 81.86 (1), γ = 83.91 (1)°; Z = 1; d_{calcd} = 1.915 g cm^{-3}; space group $P\bar{1}$. The $W_2(O\text{-}i\text{-}Pr)_6$ molecule contains a W≡W bond of distance 2.315 (2) Å and a staggered ethane-like W_2O_6 moiety with W–O = 1.87 (1) Å and W–W–O = 107 (1)° (av). The $W_4(O\text{-}i\text{-}Pr)_{12}$ molecule is centrosymmetric with a central planar $W_4(\mu\text{-}O)_4$ moiety. The W_4 moiety can be described as a distorted rhombus or flattened butterfly of W atoms with two short, 2.50 (1) Å, and two long, 2.73 (1) Å, W–W edge distances. The short W–W diagonal distance, linking the backbone W atoms, is 2.81 (1) Å. The central $W_4(\mu\text{-}O)_4O_8$ moiety has virtual C_{2h} symmetry with two terminal OR ligands per tungsten, one lying above and one below the $W_4(\mu\text{-}O)_4$ plane. The W–μ-O distances are asymmetric such that the W–O distances to the wingtip W atoms are notably shorter than those to the backbone W atoms, and this effect is most pronounced for the O-*i*-Pr ligand bridging the short W–W distance. The pure black crystalline compound $W_4(O\text{-}i\text{-}Pr)_{12}$ is obtained upon crystallization of the 1:1 mixture from hexane at ca. 0 °C and may be crystallized directly from reactions between $W_2(O\text{-}t\text{-}Bu)_6$ and *i*-PrOH (>6 equiv) in hydrocarbon solvents. The compound $W_2(O\text{-}i\text{-}Pr)_6$ can be obtained as a fine yellow powder by the removal of NMe_3 from the Lewis base adduct $W_2(O\text{-}i\text{-}Pr)_6(NMe_3)_2$ upon heating the latter under a dynamic vacuum [40 °C (10^{-4} Torr)]. The low-temperature ^{1}H NMR spectra of $W_2(O\text{-}i\text{-}Pr)_6$ and $W_4(O\text{-}i\text{-}Pr)_{12}$ in toluene-d_8 are reconcilable with the structures observed in the solid state. MO calculations employing the Fenske–Hall method on the model compound $W_4(\mu\text{-}OH)_4(OH)_8$ have been performed by assuming (i) the observed coordinates and (ii) idealized geometries of a regular rhombus, D_{2h}, and a square, D_{4h}, $W_4(\mu\text{-}OH)_4(OH)_8$ moiety. The calculated ground state for the 12-electron square cluster is a diradical and bears a striking analogy with square cyclobutadiene. The distortion from D_{4h} to D_{2h} to C_{2h} for the W_4 moiety can be understood in terms of a second-order Jahn–Teller distortion. The calculations also reveal a rationale for the asymmetry of the μ-O-*i*-Pr ligands, which favor stronger bonding to the wingtip relative to backbone tungsten atoms.

Only for certain elements of the first row are multiple bonds stable with respect to oligomerization at standard conditions (STP); i.e., N≡N is thermodynamically stable with respect to N_x, but P≡P will oligomerize to P_x.[1] Multiple bonds between transition-metal atoms are stabilized with respect to oligomerization by ligand effects, which may be steric, electrostatic, or both.[2] We have previously shown that controlled halide-for-alkoxide exchange involving $Mo_2(OR)_6$ compounds leads to the formation of tetranuclear 12-electron Mo_4 species. Examples include $Mo_4F_4(O\text{-}t\text{-}Bu)_8$,[3] $Mo_4F_2(O\text{-}i\text{-}Pr)_{10}$,[4] $Mo_4Cl_4(O\text{-}i\text{-}Pr)_8$,[4,5] and $Mo_4Br_4(O\text{-}i\text{-}Pr)_8$,[4,5] which have bisphenoid, rectangular, square, and butterfly Mo_4 units, respectively. The substitution of halide-for-alkoxide ligands, that leads to oligomerization of the $(M{\equiv}M)^{6+}$ unit, circumvents the fundamental objective of dimerizing two $M_2(OR)_6$ units. Since the initial discovery of compounds of formula $M_2(OR)_6$ for M = Mo[6] and W,[7] we have speculated about the existence of 12-electron $M_4(OR)_{12}$ compounds, but no such compound has been successfully characterized because of problems associated with obtaining crystals suitable for X-ray analysis or the ease of oxidation of the $(M{\equiv}M)^{6+}$ moiety.[8]

In this paper we describe the preparation of $W_2(O\text{-}i\text{-}Pr)_6$, its dimer $W_4(O\text{-}i\text{-}Pr)_{12}$, and the 1:1 mixture of the two, which crystallizes from dme (1,2-dimethoxyethane) solutions.[9] This work provides the first observation and characterization of a metal–metal triple bond and its 12-electron M_4 cluster. It should, of course, be recognized that coupling of M–M triple bonds, as in the formation of $Mo_4X_4(OR)_8$ compounds noted above, and coupling of quadruple bonds by condensation reactions have been previously reported.[10,11] However, in none of these instances is there an equilibrium between two dinuclear compounds and the tetranuclear cluster. In the following paper we present our studies of the dynamics of the equilibrium shown in eq 1.

$$W_4(O\text{-}i\text{-}Pr)_{12} \rightleftharpoons 2W_2(O\text{-}i\text{-}Pr)_6 \quad (1)$$

Results and Discussion

Syntheses. $W_4(O\text{-}i\text{-}Pr)_{12}$. Addition of *i*-PrOH (>6 equiv) to hydrocarbon solutions of $W_2(O\text{-}t\text{-}Bu)_6$[7] yields a dark brown solution from which black crystals of $W_4(O\text{-}i\text{-}Pr)_{12}$ can be obtained by cooling the solution to −15 °C, in ca. 60% yield (see eq 2). This

(1) (a) Steudel, R. *Chemistry of the Non-Metals*; de Gruyter: New York, 1977. (b) Greenwood, N. N.; Earnshaw, A. *Chemistry of the Elements*; Pergamon: New York, 1984. Cotton, F. A.; Wilkinson, G. *Advanced Inorganic Chemistry*; Wiley: New York, 1980.
(2) Cotton, F. A.; Walton, R. A. *Multiple Bonds Between Metal Atoms*; Wiley: New York, 1982.
(3) Chisholm, M. H.; Clark, D. L.; Huffman, J. C. *Polyhedron* **1985**, *4*, 1203.
(4) Chisholm, M. H.; Clark, D. L.; Errington, R. J.; Huffman, J. C., submitted for publication in *Inorg. Chem.*
(5) Chisholm, M. H.; Folting, K.; Errington, R. J.; Huffman, J. C. *J. Am. Chem. Soc.* **1982**, *104*, 2025.
(6) Chisholm, M. H.; Cotton, F. A.; Murillo, C. A.; Reichert, W. W. *Inorg. Chem.* **1977**, *16*, 1801.
(7) Akiyama, M.; Chisholm, M. H.; Cotton, F. A.; Extine, M. W.; Haitko, D. A.; Little, D.; Fanwick, P. E. *Inorg. Chem.* **1979**, *18*, 2266.
(8) (a) Akiyama, M.; Chisholm, M. H.; Extine, M. W.; Haitko, D. A.; Little, D.; Cotton, F. A.; Extine, M. W. *J. Am. Chem. Soc.* **1981**, *103*, 779. (b) Chisholm, M. H.; Huffman, J. C.; Smith, C. A. *J. Am. Chem. Soc.* **1986**, *108*, 222 and references therein.
(9) A preliminary report of some aspects of this work has appeared: Chisholm, M. H.; Clark, D. L.; Folting, K.; Huffman, J. C. *Angew. Chem., Int. Ed. Engl.* **1986**, *25*, 1014.
(10) McGinnis, R. N.; Ryan, T. R.; McCarley, R. E. *J. Am. Chem. Soc.* **1978**, *100*, 7900.
(11) McCarley, R. E.; Ryan, T. R.; Torardi, C. C. *ACS Symp. Ser.* **1981**, *No. 155*, 44.

0002-7863/87/1509-7750$01.50/0

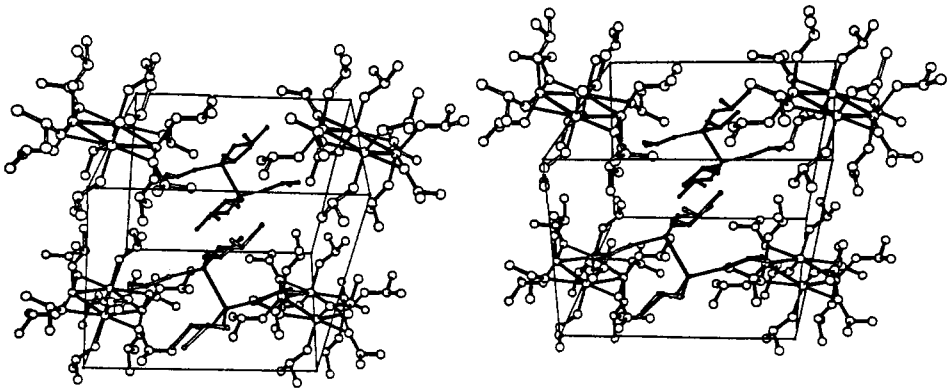

Figure 1. Stereoview of the unit cell containing $W_4(O\text{-}i\text{-}Pr)_{12}$ and $W_2(O\text{-}i\text{-}Pr)_6$ in the ratio 1:1. The ball-and-stick model uses different size balls for the W_2- and W_4-containing compounds.

Table I. Fractional Coordinates and Isotropic Thermal Parameters for $W_4(O\text{-}i\text{-}Pr)_{12}$:$W_2(O\text{-}i\text{-}Pr)_6$

atom	10^4x	10^4y	10^4z	$10B_{iso}$
W(1)	3851 (1)	10110 (1)	9997 (1)	35
W(2)	4928 (1)	8353 (1)	9370 (1)	37
O(3)	3354 (12)	10449 (12)	8648 (12)	45
C(4)	2928 (27)	11249 (24)	8100 (26)	78
C(5)	1818 (28)	11035 (41)	7844 (35)	141
C(6)	3655 (36)	11437 (30)	7070 (27)	104
O(7)	2864 (12)	9901 (13)	11308 (13)	51
C(8)	2360 (21)	9154 (21)	11827 (26)	69
C(9)	1129 (22)	9530 (24)	12016 (35)	95
C(10)	2799 (28)	8923 (26)	12860 (22)	80
O(11)	3461 (11)	11772 (13)	10588 (13)	49
C(12)	2559 (19)	12405 (21)	11235 (26)	63
C(13)	2779 (22)	13444 (25)	11472 (24)	70
C(14)	1459 (20)	12250 (23)	10925 (30)	77
O(15)	4732 (11)	7641 (11)	10767 (15)	51
C(16)	4745 (21)	6589 (23)	10803 (26)	67
C(17)	3621 (25)	6299 (30)	11165 (28)	84
C(18)	5621 (23)	6184 (25)	11458 (25)	74
O(19)	5186 (13)	8289 (14)	7794 (16)	64
C(20)	5370 (24)	8794 (28)	6897 (20)	79
C(21)	6504 (24)	8476 (24)	6242 (20)	66
C(22)	4577 (25)	8569 (31)	6053 (23)	85
O(23)	3425 (16)	8259 (33)	9314 (18)	168
C(24)	2691 (29)	7945 (46)	8514 (29)	145
C(25)	1544 (31)	8217 (62)	9051 (39)	226
C(26)	3017 (46)	6852 (48)	8103 (73)	226
W(27)	10532 (1)	4431 (1)	4292 (1)	42
O(28)	10222 (12)	4922 (14)	2943 (13)	54
C(29)	9662 (18)	5747 (20)	2499 (20)	49
C(30)	8949 (21)	5333 (26)	1696 (24)	69
C(31)	10520 (23)	6389 (24)	1915 (21)	62
O(32)	12022 (11)	4456 (15)	4485 (14)	58
C(33)	12623 (19)	5062 (22)	5149 (19)	52
C(34)	13215 (20)	5806 (24)	4456 (24)	64
C(35)	13380 (23)	4350 (23)	5712 (24)	66
O(36)	10081 (22)	3112 (16)	4466 (26)	121
C(37)	9767 (33)	2325 (24)	4747 (32)	93
C(38)	8893 (23)	1848 (24)	4166 (24)	66
C(39)	10516 (27)	1605 (22)	5246 (25)	72

preparation is identical with that described previously for the compound of proposed formula $[W(O\text{-}i\text{-}Pr)_3]_4$.[8]

$$W_2(O\text{-}t\text{-}Bu)_6 + 6\,i\text{-PrOH} \xrightarrow[\text{hexane}]{0\ ^\circ C} {}^1/_2W_4(O\text{-}i\text{-}Pr)_{12} + 6\,t\text{-BuOH} \quad (2)$$

$W_4(O\text{-}i\text{-}Pr)_{12}$:$W_2(O\text{-}i\text{-}Pr)_6$. If the addition of *i*-PrOH to $W_2(O\text{-}t\text{-}Bu)_6$ is carried out in the presence of the weakly ligating solvent dme (dme = 1,2-dimethoxyethane), then crystals obtained from the solution at ca. 0 °C represent a 1:1 mixture of the dinuclear and tetranuclear compounds. Subsequent recrystallization from hexane or toluene at ca. 0 °C yields only the black crystalline tetranuclear compound $W_4(O\text{-}i\text{-}Pr)_{12}$.

$W_2(O\text{-}i\text{-}Pr)_6$. In order to obtain this compound in a pure state, i.e. free from contamination with the tetranuclear compound, we have had to prepare the lightly ligated compound $W_2(O\text{-}i\text{-}Pr)_6(NMe_3)_2$. This is obtained from eq 3 as an orange-brown crystalline solid.

$$W_2(NMe_2)_6 + i\text{-PrOH (>6 equiv)} + NMe_3 \text{ (excess)} \xrightarrow[\text{hexane}]{0\ ^\circ C} W_2(O\text{-}i\text{-}Pr)_6(NMe_3)_2 + 6HNMe_2 \quad (3)$$

The trimethylamine is only weakly bonded to tungsten and at room temperature may be removed under a dynamic vacuum. Heating $W_2(O\text{-}i\text{-}Pr)_6(NMe_3)_2$ to ca. 40 °C (10^{-4} Torr) leads to the formation of $W_2(O\text{-}i\text{-}Pr)_6$ as a fine yellow powder as outlined in eq 4.

$$W_2(O\text{-}i\text{-}Pr)_6(NMe_3)_2 \xrightarrow{40\ ^\circ C\ (10^{-4}\ \text{Torr})} W_2(O\text{-}i\text{-}Pr)_6 + 2NMe_3 \quad (4)$$

Solid-State and Molecular Structures. The sample examined in this study was obtained by crystallization from dme. In the space group $P\bar{1}$, the asymmetric unit contains two halves of two different centrosymmetric tungsten compounds. A stereoview of the unit cell is given in Figure 1. The planar tetranuclear compound $W_4(O\text{-}i\text{-}Pr)_{12}$ is numbered W(1) through C(26), and the dinuclear compound $W_2(O\text{-}i\text{-}Pr)_6$ is numbered W(27) through C(39). Atomic positional parameters are given in Table I.

$W_2(O\text{-}i\text{-}Pr)_6$. A view of the dinuclear compound, giving the atom number scheme, is given in Figure 2, and a view looking down the W–W bond is given in Figure 3. In both figures, ball-and-stick drawings are accompanied by space-filling model drawings, which reveal that the metal atoms are exposed; i.e., $W_2(O\text{-}i\text{-}Pr)_6$ is coordinatively unsaturated. This is, in fact, the first structural characterization of an unligated $W_2(OR)_6$ compound. The general features of the structure are as now anticipated for a member of the $X_3M{\equiv}MX_3$ class of compounds.[12,13]

Table II. Selected Bond Distances (Å) and Angles (deg) for the $W_2(O\text{-}i\text{-}Pr)_6$ Molecules

atom	atom	distance
W(27)	W(27)′	2.3150 (20)
W(27)	O(28)	1.873 (16)
W(27)	O(32)	1.880 (14)
W(27)	O(36)	1.861 (22)

atom	atom	atom	angle
W(27)′	W(27)	O(28)	106.3 (5)
W(27)′	W(27)	O(32)	107.3 (5)
W(27)′	W(27)	O(36)	106.5 (10)
O(28)	W(27)	O(32)	113.1 (7)
O(28)	W(27)	O(36)	111.8 (9)
O(32)	W(27)	O(36)	111.5 (9)
W(27)	O(28)	C(29)	142.9 (15)
W(27)	O(32)	C(33)	136.8 (15)
W(27)	O(36)	C(37)	170 (3)

(12) Chisholm, M. H.; Cotton, F. A. *Acc. Chem. Res.* **1978**, *11*, 356.
(13) Chisholm, M. H. *Angew. Chem., Int. Ed. Engl.* **1986**, *25*, 21.

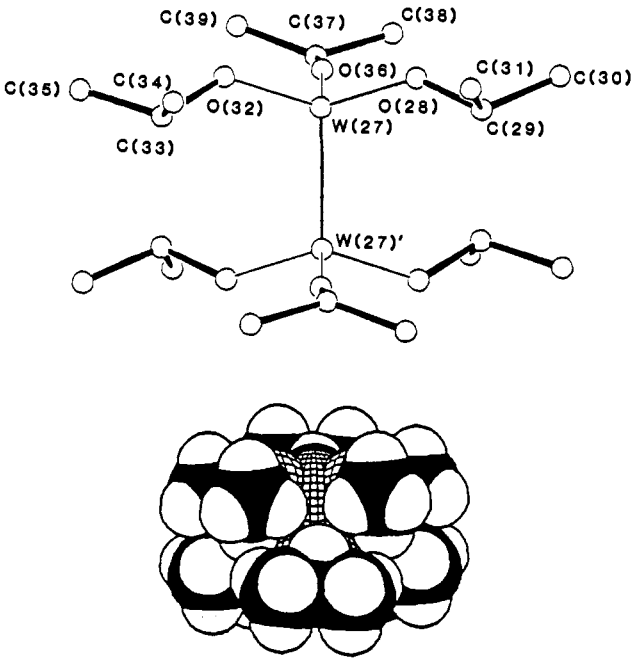

Figure 2. View of the $W_2(O\text{-}i\text{-}Pr)_6$ molecule emphasizing the staggered ethane-like geometry and giving the atom number scheme used in the tables. A corresponding space-filling model diagram of this same view is shown at the bottom.

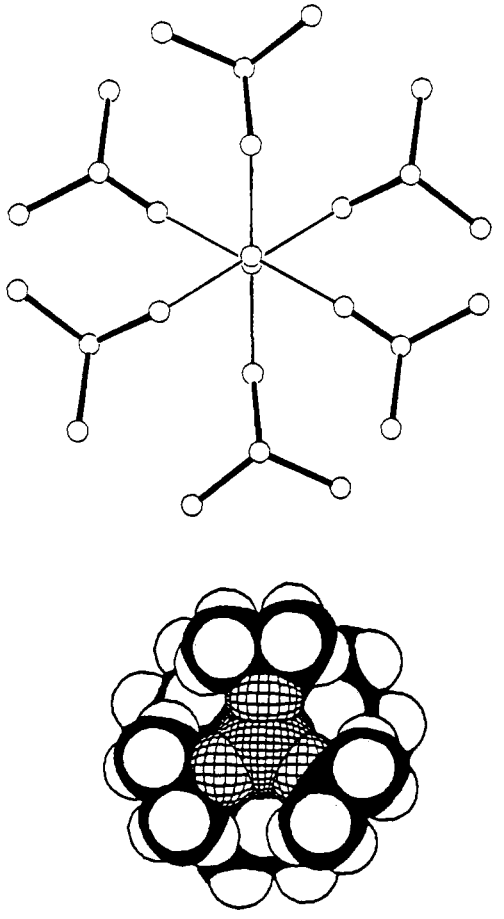

Figure 3. View of the $W_2(O\text{-}i\text{-}Pr)_6$ molecule looking down the metal–metal bond and emphasizing the staggered ethane-like geometry. A corresponding space-filling model diagram of this same view is shown at the bottom.

Selected bond distances and bond angles are given in Table II.

The W–W distance, 2.31 Å, is indicative of a W≡W bond and is only slightly shorter than that seen in its pyridine adduct $W_2(O\text{-}i\text{-}Pr)_6(py)_2$, 2.33 Å.[7] The W–O distances, 1.87 Å (av), are similar to the Mo–O distances seen in $Mo_2(OCH_2\text{-}t\text{-}Bu)_6$, 1.88 Å (av),[6] and are indicative of strong oxygen-to-metal π-bonding.[14] The W–O–C angles range from 137 to 170°, and the shortest W–O distance, W(27)–O(36), involves the largest W–O–C angle, though the range in W–O distances is within 3σ. In the ground state, the conformation with six methyne protons proximal to the W≡W bond is preferred. The mean W–W–O and O–W–O angles of 106.7 and 112.1°, respectively, may be compared with the Mo–Mo–O and O–Mo–O angles of 103.1 and 115.0° in $Mo_2(OCH_2\text{-}t\text{-}Bu)_6$.[6]

Table III. Selected Bond Distances (Å) for the $W_4(O\text{-}i\text{-}Pr)_{12}$ Molecule

atom	atom	distance
W(1)	W(1)′	2.8068 (21)
W(1)	W(2)	2.5018 (14)
W(1)	W(2)′	2.7329 (14)
W(1)	O(3)	1.891 (14)
W(1)	O(7)	1.913 (15)
W(1)	O(11)	2.184 (16)
W(1)	O(23)	2.59 (4)
W(2)′	O(11)	1.976 (14)
W(2)	O(15)	1.987 (17)
W(2)	O(19)	1.885 (20)
W(2)	O(23)	1.872 (18)

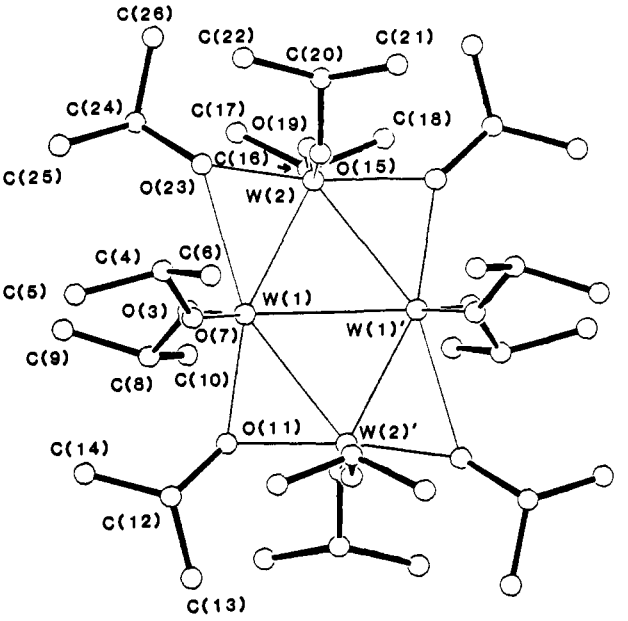

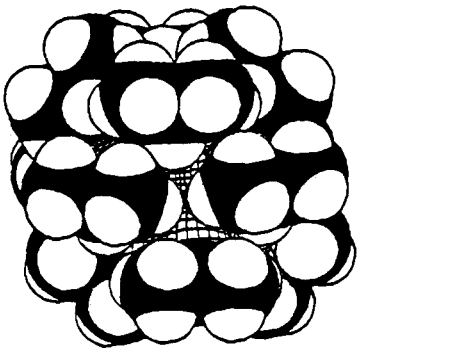

Figure 4. View of the $W_4(\mu\text{-}O\text{-}i\text{-}Pr)_4(O\text{-}i\text{-}Pr)_8$ molecule emphasizing the rhomboidal W_4 unit and giving the atom number scheme used in the tables. A corresponding space-filling model diagram of this same view is shown at the bottom.

(14) Chisholm, M. H. *Polyhedron* **1983**, *2*, 681.

Table IV. Selected Bond Angles (deg) for the $W_4(O\text{-}i\text{-}Pr)_{12}$ Molecule

atom	atom	atom	angle
W(1)	W(1)′	W(2)′	61.65 (4)
W(1)′	W(1)′	O(3)	116.9 (4)
W(1)′	W(1)	O(7)	120.2 (5)
W(1)′	W(1)	O(11)	99.4 (4)
W(1)′	W(1)	O(23)	104.7 (5)
W(2)′	W(1)′	W(2)	115.33 (5)
W(2)′	W(1)	O(3)	107.4 (4)
W(2)′	W(1)	O(7)	106.2 (5)
W(2)′	W(1)	O(11)	45.7 (4)
W(2)′	W(1)	O(23)	158.4 (5)
O(3)	W(1)	O(7)	122.9 (6)
O(3)	W(1)	O(11)	87.2 (6)
O(3)	W(1)	O(23)	82.2 (7)
O(7)	W(1)	O(11)	84.6 (6)
O(7)	W(1)	O(23)	83.1 (7)
O(11)	W(1)	O(23)	155.9 (6)
W(1)	W(2)	W(1)′	64.67 (5)
W(1)′	W(2)	O(11)′	52.3 (5)
W(1)	W(2)	O(15)′	101.6 (5)
W(1)	W(2)	O(19)	105.1 (5)
W(1)	W(2)	O(23)	71.1 (13)
O(11)′	W(2)	O(15)	89.0 (6)
O(11)′	W(2)	O(19)	90.6 (7)
O(11)′	W(2)	O(23)	171.6 (14)
O(15)	W(2)	O(19)	150.2 (7)
O(15)	W(2)	O(23)	87.0 (8)
O(19)	W(2)	O(23)	89.3 (8)
W(1)	O(3)	C(4)	144.3 (17)
W(1)	O(7)	C(8)	142.2 (17)
W(1)	O(11)	W(2)′	82.0 (6)
W(1)	O(11)	C(12)	135.9 (14)
W(2)	O(11)	C(12)	132.6 (14)
W(2)	O(15)	C(16)	124.8 (18)
W(2)	O(19)	C(20)	147.7 (21)
W(1)	O(23)	W(2)	65.9 (10)
W(1)	O(23)	C(24)	130 (3)
W(2)	O(23)	C(24)	140.1 (23)

$W_4(O\text{-}i\text{-}Pr)_{12}$. Selected bond distances and bond angles are given in Tables III and IV, respectively. A view of the molecule emphasizing the centrosymmetric rhomboidal W_4 unit and giving the atom-numbering scheme used in the tables is shown in Figure 4 along with a space-filling model diagram of the same view. Two alternate views of the $W_4(\mu\text{-}O\text{-}i\text{-}Pr)_4(O\text{-}i\text{-}Pr)_8$ molecule looking parallel to the W_4-containing plane and emphasizing the approximately trigonal-bipyramidal and square-based-pyramidal WO_4 coordination geometry about the backbone and wingtip tungsten atoms are shown in Figures 5 and 6, respectively.

The $W_4(\mu\text{-}O\text{-}i\text{-}Pr)_4(O\text{-}i\text{-}Pr)_8$ molecule consists of a distorted rhombus (or flattened butterfly) of tungsten atoms with two short W–W distances of 2.50 Å [W(1)–W(2) and W(1)′–W(2)′] and two longer distances of 2.73 Å [W(1)–W(2)′ and W(1)′–W(2)] and with a diagonal (or backbone) distance of 2.81 Å [W(1)–W(1)′], which is still worthy of mention with regards to metal–metal bonding. The asymmetry in the W–W distances around the edge of the rhombus is quite striking and rather suggestive of alternating W–W double and single bonds for the short and long edges, respectively. The short W–W distance of 2.50 Å is clearly indicative of some degree of multiple bonding and can be compared to the W–W double bond distances of 2.45 Å in $W_4H_2(O\text{-}i\text{-}Pr)_{14}$,[8a] 2.53 Å in $W_2(\mu\text{-}CO)(O\text{-}t\text{-}Bu)_6$,[15] and 2.48 Å in $W_2Cl_4(OMe)_4(MeOH)_2$.[16]

There are four edge-shared alkoxide ligands whose oxygen atoms are contained in the W_4 plane while the remaining eight alkoxides are terminal, two per tungsten atom, with four lying above and four below the W_4 plane. The local WO_4 geometry around the backbone tungsten atoms may be viewed in terms of distorted trigonal-bipyramidal fragments in which one equatorial ligand is missing. This site is directed toward the center of the cluster, and the terminal and bridging alkoxide ligands make up the remaining equatorial and axial positions, respectively. When viewed in this fashion, it can be seen that the equatorial and axial O–W–O angles are 123 and 156°, respectively. By comparison, the local WO_4 coordination geometry about the wingtip tungsten atoms is more appropriately viewed in terms of distorted square-based-pyramidal fragments in which the apical ligand is missing. This site is directed toward the center of the cluster, with the terminal and bridging alkoxides making up the remaining basal sites, and it is seen that the O–W–O angles are 150 and 172° for the terminal and bridging alkoxides, respectively. Two views of the $W_4(\mu\text{-}O\text{-}i\text{-}Pr)_4(O\text{-}i\text{-}Pr)_8$ molecule that emphasize the local trigonal-bipyramidal and square-based-pyramidal coordination geometries are shown in Figures 5 and 6, respectively.

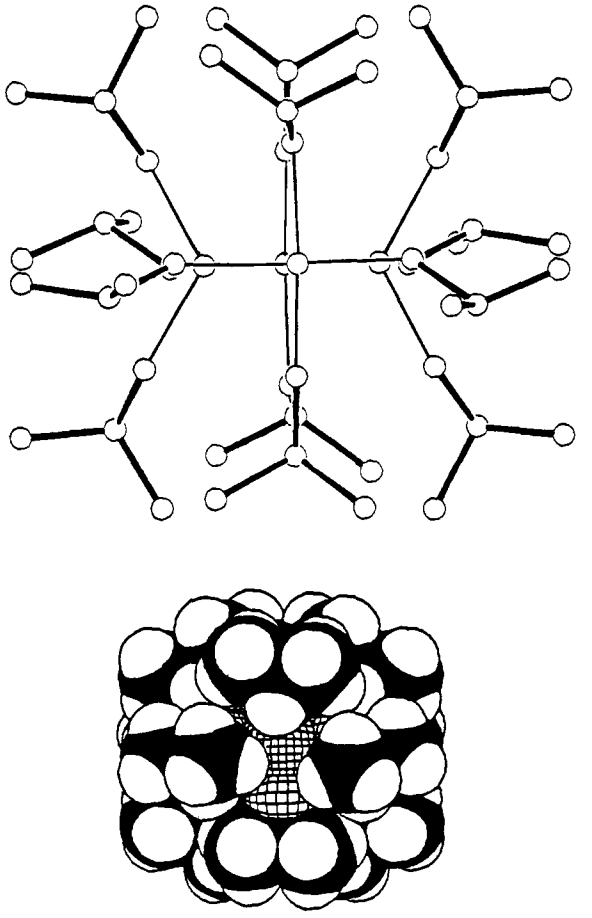

Figure 5. View of the $W_4(\mu\text{-}O\text{-}i\text{-}Pr)_4(O\text{-}i\text{-}Pr)_8$ molecule looking directly at the wingtip tungsten atoms and parallel to the edge of the W_4 rhombus. This view emphasizes both the planarity of the $W_4(\mu\text{-}O)_4$ core and the local trigonal-bipyramidal coordination geometry about the backbone W atoms.

The terminal W–O distances range from 1.88 to 1.99 Å, are within the "normal" range of four-coordinate W(III)–O terminal distances, and can be compared to those of $W_2(O\text{-}i\text{-}Pr)_6(py)_2$, which range from 1.86 to 2.04 Å.[7] All of the bridging alkoxide ligands form asymmetric bridges, and their oxygen atoms are contained within the W_4 plane. The alkoxide bridges involving the long (2.73 Å) W–W edge exhibit W–O distances of 2.18 and 1.97 Å to the backbone and wingtip tungsten atoms, respectively. Of particular note is the asymmetry of the bridges involving the short W–W distance (2.50 Å) in which the W–O distances are 1.87 and 2.59 Å to the wingtip and backbone tungsten atoms, respectively. The short W–O distance of 1.87 Å is, in fact, within the range found for the terminal W–O distances in $W_2(O\text{-}i\text{-}Pr)_6$ and is suggestive of significant oxygen-to-metal π-donation.[14] The long W–O distance, 2.59 Å, is approaching the length that we have designated "semibridging".[17]

(15) Chisholm, M. H.; Hoffman, D. M.; Huffman, J. C. *Organometallics* **1985**, *4*, 986.

(16) Anderson, L. B.; Cotton, F. A.; DeMarco, D.; Fang, A.; Ilsley, W. H.; Kolthammer, B. W. S.; Walton, R. A. *J. Am. Chem. Soc.* **1981**, *103*, 1034, 5078.

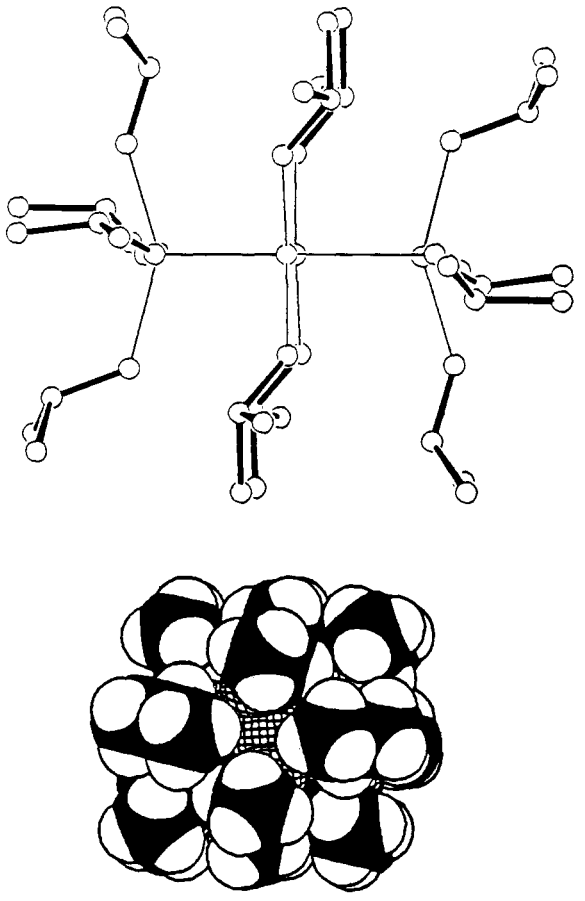

Figure 6. View of the $W_4(\mu\text{-O-}i\text{-Pr})_4(\text{O-}i\text{-Pr})_8$ molecule looking directly at the backbone tungsten atoms and parallel to the edge of the W_4 rhombus. This view emphasizes both the planarity of the $W_4(\mu\text{-O})_4$ core and the local square-based-pyramidal coordination geometry about the wingtip tungsten atoms.

In summary, the $W_4(\mu\text{-O-}i\text{-Pr})_4(\text{O-}i\text{-Pr})_8$ cluster may be viewed as a distorted rhomboidal W_4 unit with alternating double and single W–W bonds along the short and long edges, respectively. The backbone tungsten atoms are best described as having a distorted trigonal-bipyramidal coordination geometry with short equatorial and long axial W–O bonds, while the wingtip tungsten atoms have a distorted square-based-pyramidal coordination geometry with relatively short basal W–O bonds. These statements are pictorially represented in the valence bond description shown in I.

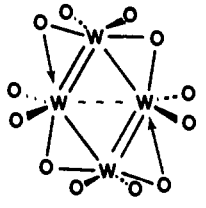

I

Electronic Structure and Bonding in the Tetranuclear Rhomboidal Cluster. The solid-state molecular structure of $W_4(\text{O-}i\text{-Pr})_{12}$ possesses several fascinating questions as to whether one can account for both the distorted nature of the rhomboidal W_4 framework and the asymmetric nature of the four W–O bridges. It will be demonstrated in this section that these questions may be answered in a very satisfying way with the aid of approximate molecular orbital calculations. We have employed the Fenske–Hall molecular orbital method[18] to obtain numerical results, which allow for the understanding of both the rhomboidal distortion within the cluster framework and the asymmetric nature of the W–O bridges in terms of a second-order Jahn–Teller effect.

(17) Chisholm, M. H.; Folting, K.; Huffman, J. C.; Kirkpatrick, C. C. *J. Chem. Soc., Chem. Commun.* **1982**, 188.

Table V. Relative Orbital Energies and Atomic Orbital Populations for the Primarily 5d Valence Molecular Orbitals of D_{4h} $[W_4]^{12+}$

orbital	rel E, eV	% contribution[a] z^2	x^2-y^2	xy	xz	yz	s	p
$1a_{1g}$	−19.00	84	13				0	4
$1b_{2g}$	−16.95				100			0
$1a_{2u}$	−16.20					97		3
$1b_{1u}$	−15.33			100				
$2a_{1g}$	−14.70	12	86				2	0
$1e_u$	−14.23	2	36		59		1	2
$1e_g$	−13.61			59		39		2
$2e_u$	−9.82	67	15		5		1	2
$3e_u$	−7.31	17	45		33		1	4
$2e_g$	−6.51			29		57		14
$1b_{1g}$	−6.14	41	59				0	0
$1b_{2u}$	−5.55					87		13
$1a_{1u}$	−2.12			100				
$2b_{1g}$	−1.23	36	27				10	27
$1a_{2g}$	0.00				89			11

[a] Blank entries are zero by symmetry.

The approach chosen for this study employs the "clusters in molecules" formalism, which has proven successful in understanding both the metal–metal and metal–ligand bonding in related metal atom cluster compounds.[19-22] In the clusters in molecules approach, the molecular orbitals of the entire molecule are expressed in a basis set composed of the ligand atomic orbitals and the canonical valence molecular orbitals of the metal cluster framework. In this fashion one can examine how the Mulliken populations of the canonical valence orbitals of the cluster framework vary with different ligand environments yet maintain the central M_4 cluster unit as the focus of discussion. In order to account for the distorted nature of the rhomboidal cluster unit, we sought to examine first a symmetrical D_{4h} square cluster to see what inherent instability might be present in the higher symmetry cluster. To make the computation more tractable, the bonding in a model compound of formula $W_4(\mu\text{-OH})_4(\text{OH})_8$ in an idealized D_{4h} (square W_4) geometry was investigated. The question of how bridging and terminal ligands bond to the D_{4h} W_4^{12+} core will be addressed by examination of the electronic structure of the D_{4h} W_4^{12+} core plus each degree of ligation separately. Accordingly, separate calculations were performed for $W_4(\mu\text{-OH})_4^{8+}$ and the complete $W_4(\mu\text{-OH})_4(\text{OH})_8$ cluster, and following convergence, the results were transformed into a basis of the canonical orbitals of W_4^{12+}. To implement the clusters in molecules formalism, it is useful to first discuss the bonding in the symmetric D_{4h} W_4^{12+} cluster core.

***D*$_{4h}$ W_4^{12+} Cluster Core.** In discussing the idealized D_{4h} W_4^{12+} cluster core, it is convenient to employ a right-handed local Cartesian coordinate system on each metal atom in which the z axis points toward the center of the square, the x axis lies in the plane of the square, and the y axis is perpendicular to the plane. Under D_{4h} symmetry, the W 5d atomic orbitals in this coordinate system transform as the following irreducible representations:

$$z^2: \; a_{1g} + b_{1g} + e_u$$

$$x^2 - y^2: \; a_{1g} + b_{1g} + e_u$$

$$xz: \; a_{2g} + b_{2g} + e_u$$

$$yz: \; a_{2u} + b_{2u} + e_g$$

$$xy: \; a_{1u} + b_{1u} + e_g$$

(18) Hall, M. B.; Fenske, R. F. *Inorg. Chem.* **1972**, *11*, 768.
(19) Bursten, B. E.; Cotton, F. A.; Hall, M. B.; Najjar, R. C. *Inorg. Chem.* **1982**, *21*, 302.
(20) Chisholm, M. H.; Cotton, F. A.; Fang, A.; Kober, E. M. *Inorg. Chem.* **1984**, *23*, 749.
(21) Cotton, F. A.; Fang, A. *J. Am. Chem. Soc.* **1982**, *104*, 113.
(22) Bursten, B. E.; Chisholm, M. H.; Clark, D. L., submitted for publication in *Inorg. Chem.*

Table VI. Selected Mulliken Populations of the Canonical Orbitals of D_{4h} $[W_4]^{12+}$ for $[W_4(\mu\text{-OH})_4]^{8+}$ and $W_4(\mu\text{-OH})_4(OH)_8$ Clusters

orbital	$[W_4]^{12+}$	$[W_4(\mu\text{-OH})_4]^{8+}$	$W_4(\mu\text{-OH})_4(OH)_8$
$1a_{1g}$	2.00	1.57	1.56
$1b_{2g}$	2.00	1.99	1.98
$1a_{2u}$	2.00	2.00	1.86
$1b_{1u}$	2.00	0.90	0.72
$2a_{1g}$	2.00	0.98	0.91
$1e_u$	2.00	2.38	3.31
$1e_g$	0.00	3.83	2.55
$2e_u$	0.00	1.02	1.28
$3e_u$	0.00	0.15	1.23
$2e_g$	0.00	0.90	0.83
$1b_{1g}$	0.00	0.10	0.48
$1b_{2u}$	0.00	0.00	0.42
$3a_{1g}$	0.00	0.11	0.57

The forms of the metal cluster orbitals are determined by a calculation on the D_{4h} W_4^{12+} moiety alone, which gives rise to 36 molecular orbitals, the lowest 20 of which are derived from primarily metal d atomic orbitals. The relative energies and Mulliken percent characters of the primarily 5d molecular orbitals of W_4^{12+} are given in Table V. From the table it is clear that our choice of local coordinates results in molecular orbitals that retain, to a large extent, the character of primarily one type of atomic orbital, even when mixing is allowed by symmetry. The 12 valence electrons are expected to occupy the $1a_{1g}$, $1a_{2u}$, $1b_{2g}$, $1b_{1u}$, $2a_{1g}$, and $1e_u$ orbitals, which are depicted qualitatively in II. The $1a_{1g}$ and $2a_{1g}$ orbitals may be regarded as the σ-bonding

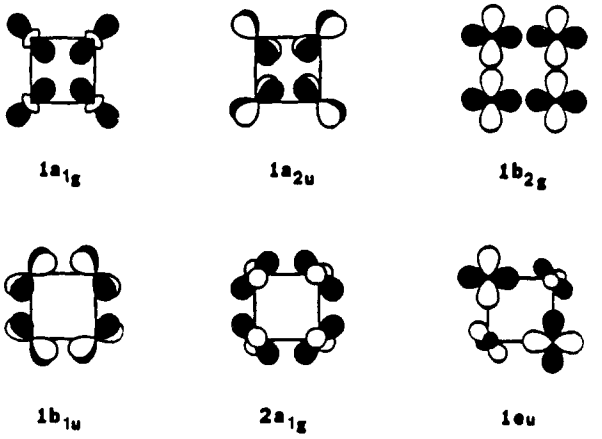

II

combinations of the W $5d_{z^2}$ and $5d_{x^2-y^2}$ AO's, respectively, although Table V shows that these AO's are slightly mixed in W_4^{12+}. The $1a_{2u}$ and $1b_{1u}$ orbitals may be regarded as the in-phase π-bonding combinations of the W $5d_{yz}$ and $5d_{xy}$ AO's, respectively. The $1b_{2g}$ orbital is the in-phase σ-bonding combination of W $5d_{xz}$ AO's, and finally, the $1e_u$ orbital is a mixture of primarily W $5d_{xz}$ with some W $5d_{x^2-y^2}$ contribution.

Edge-Bridging Ligands. The correlation of energy levels of W_4^{12+}, $W_4(\mu\text{-OH})_4^{8+}$, and the complete $W_4(\mu\text{-OH})_4(OH)_8$ molecule under D_{4h} symmetry is shown in Figure 7. The Mulliken populations of the canonical orbitals of D_{4h} W_4^{12+} for each degree of perturbation are listed in Table VI and may be used as a guide toward understanding the correlation diagram. From the correlation diagram (Figure 7), it can be seen that virtually all of the canonical orbitals of W_4^{12+} are destabilized by interaction with the bridging ligands. For virtually each symmetry type some metal–metal bonding is sacrificed to facilitate metal–ligand bonding, and the magnitude of destabilization of these metal-based orbitals can be taken as a rough measure of the stabilizing interaction occurring in lower lying metal–ligand bonding orbitals. A major portion of the metal–ligand bonding occurs via donation from the bridging ligand orbitals into empty, nonbonding, and antibonding orbitals of W_4^{12+}.

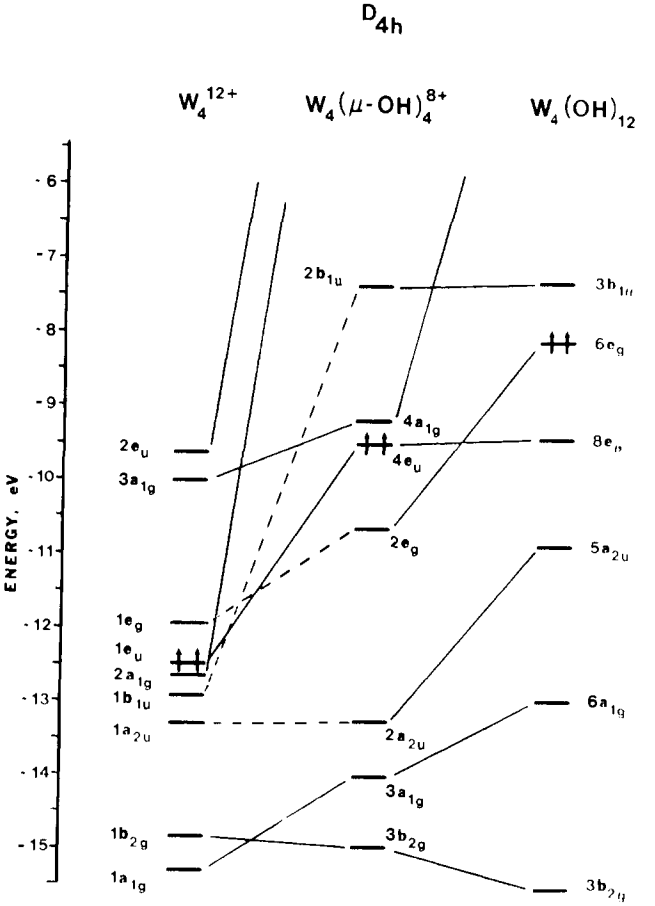

Figure 7. Correlation diagram tracing the perturbations of the primarily metal–metal bonding orbitals in D_{4h} W_4^{12+} (left) as ligation occurs through (1) introduction of four μ-OH ligands (center) and (2) introduction of eight terminal OH ligands (right). The HOMO for each degree of perturbation is denoted by arrows.

In the $(\mu\text{-OH})_4^{4-}$ ligand set there exists a subset of four oxygen pσ lone-pair orbitals that transform as $a_{1g} + b_{2g} + e_u$ irreducible representations and a subset of four oxygen pπ lone-pair orbitals that lie parallel to the W_4 plane and transform as $a_{2g} + b_{1g} + e_u$ irreducible representations in the D_{4h} point group. Together, these two types of lone-pair orbitals may be used to form eight W–μ-O σ bonds with W_4^{12+} orbitals of the same symmetry. The perturbations imposed on the W_4^{12+} orbitals via these σ interactions are illustrated in Figure 7 in the form of solid lines connecting the W_4^{12+} orbitals to their counterparts in $W_4(\mu\text{-OH})_4^{8+}$. There is a secondary metal–ligand π interaction that occurs between the edge-bridging ligands and W_4^{12+} orbitals. The set of four oxygen pπ lone-pair orbitals of the $(\mu\text{-OH})_4^{4-}$ ligand set, which lie perpendicular to the W_4 plane (those not used in forming the eight W–μ-O σ bonds), are available for W–O π-bonding. This set of pπ lone-pair orbitals transforms as $a_{2u} + b_{1u} + e_g$ irreducible representations in the D_{4h} point group and can form π bonds with W_4^{12+} orbitals of the same symmetry. In the correlation diagram of Figure 7, dashed lines are used to trace the perturbations imposed on the W_4^{12+} orbitals as a result of this π interaction.

First, let us examine the behavior of the metal–metal bonding orbitals of the above symmetry types, which were occupied in the "naked" W_4^{12+} cluster. In particular, the $2a_{1g}$ and $1b_{1u}$ orbitals are directed to the site of the incoming edge-bridging ligands and are removed from the frontier region by σ and π interaction, respectively, to form $W_4(\mu\text{-OH})_4^{8+}$. The $1e_g$ orbital, which was unoccupied in W_4^{12+}, accommodates these four electrons in the $W_4(\mu\text{-OH})_4^{8+}$ fragment, and the dramatic destabilization of the $1b_{1u}$ and $2a_{1g}$ orbitals of W_4^{12+} can be seen in the correlation diagram shown in Figure 7. These observations are further amplified by the Mulliken populations of the canonical orbitals of W_4^{12+} in the $W_4(\mu\text{-OH})_4^{8+}$ fragment given in Table VI. From

the table it can be seen that removal of the $1b_{1u}$ and $2a_{1g}$ orbitals of W_4^{12+} from the metal–metal bonding manifold results in the transfer of charge out of the $1b_{1u}$ and $2a_g$ orbitals as revealed by the dramatic decrease in Mulliken population of the $1b_{1u}$ and $2a_{1g}$ orbitals of W_4^{12+} in $W_4(\mu\text{-}OH)_4^{8+}$. Second, the increase in the Mulliken population of the $1e_g$ orbital of W_4^{12+} in $W_4(\mu\text{-}OH)_4^{8+}$ reveals the transfer of charge into that orbital as a result of removal of the $2a_{1g}$ and $1b_{1u}$ orbitals from the metal–metal cluster bonding manifold. Finally, the σ interaction of the edge-bridging ligand set promotes a rehybridization of a_{1g} and e_u metal–metal framework bonding orbitals. Recall that in W_4^{12+} the W $5d_{z^2}$ and $5d_{x^2-y^2}$ atomic orbitals were slightly mixed in the $1a_{1g}$ and $2a_{1g}$ molecular orbitals and that W $5d_{x^2-y^2}$ atomic orbital character was spread over several molecular orbitals of e_u symmetry (Table V). The edge-bridging ligand σ interaction forces a rehybridization of the metal-based a_{1g} and e_u orbitals in an attempt to preserve metal–metal cluster bonding. The rehybridization induced by the edge-bridging σ interaction removes $d_{x^2-y^2}$ atomic orbital character from occupied metal–metal cluster bonding orbitals. When the results for $W_4(\mu\text{-}OH)_4^{8+}$ are transformed back into an atomic orbital basis, the resulting $3a_{1g}$ orbital is found to be composed of almost entirely W $5d_{z^2}$ atomic orbital character. The removal of the W $5d_{x^2-y^2}$ component from the $1a_{1g}$ orbital is revealed as a decrease in the Mulliken population of the $1a_{1g}$ orbital of W_4^{12+} in $W_4(\mu\text{-}OH)_4^{8+}$ (Table VI). In a similar fashion, the removal of the W $5d_{x^2-y^2}$ component from e_u orbitals results in a mixing of the $1e_u$ and $2e_u$ orbitals of W_4^{12+} in $W_4(\mu\text{-}OH)_4^{8+}$. The resulting $4e_u$ orbital of $W_4(\mu\text{-}OH)_4^{8+}$ is now a mixture of W $5d_{xz}$ and $5d_{z^2}$ atomic orbital character. As a result, the four electrons in the $4e_u$ orbital of $W_4(\mu\text{-}OH)_4^{8+}$ are spread out in the Mulliken populations (Table VI) over the $1e_u$ and $2e_u$ orbitals of W_4^{12+} in $W_4(\mu\text{-}OH)_4^{8+}$. Although the net effect of edge-bridging ligation is a rehybridization and destabilization of the manifold of metal–metal cluster bonding orbitals, the metal–metal bonding is preserved despite the introduction of metal–ligand bonding.

Terminal Ligands. The influence of the terminal ligands on the W_4^{12+} core is not all that different from the bridging ligands just discussed although they do carry different symmetry constraints. Again, a major portion of the metal–ligand bonding occurs via donation from the terminal ligand orbitals into empty, nonbonding, and antibonding framework orbitals of W_4^{12+}. In terms of the occupied metal–metal cluster bonding orbitals, it can be seen from the correlation diagram in Figure 7 that the $3a_{1g}$, $2a_{2u}$, and $2e_g$ orbitals of $W_4(\mu\text{-}OH)_4^{8+}$ are all destabilized as a result of interaction to form the complete $W_4(\mu\text{-}OH)_4(OH)_8$ cluster. These three orbitals are all directed toward the terminal ligands and undergo a rehybridization involving a mixing of virtual W 6s and 6p atomic orbitals. The e_g metal–metal cluster bonding orbital is pushed up above the e_u orbital and is only doubly occupied in D_{4h} $W_4(\mu\text{-}OH)_4(OH)_8$, and this shows up as a decrease in the Mulliken population of the $1e_g$ orbital of W_4^{12+} in $W_4(\mu\text{-}OH)_4(OH)_8$ as compared to that for $W_4(\mu\text{-}OH)_4^{8+}$. From the Mulliken populations of the complete cluster, it is clear that the populations closely resemble those of $W_4(\mu\text{-}OH)_4^{8+}$ and illustrate the dominant role of edge-bridging metal–ligand bonding interactions.

Metal–Metal Cluster Bonding and Second-Order Jahn–Teller Instability in D_{4h} $W_4(\mu\text{-}OH)_4(OH)_8$. Now that the effects of the various ligand sets on the D_{4h} W_4^{12+} cluster core have been established, we are in a position to take a closer examination of the nature of metal–metal cluster bonding in the complete $W_4(\mu\text{-}OH)_4(OH)_8$ cluster. These metal–metal bonding orbitals will, of course, be qualitatively similar to those of W_4^{12+} with the exception that some have undergone ligand-induced rehybridization. The important new orbital that has been introduced into the metal–metal bonding picture as a result of the removal of the $2a_{1g}$ and $1b_{1u}$ orbitals of W_4^{12+} is the $6e_g$ HOMO, which is illustrated qualitatively in III. The 12 electrons expected for tungsten will give rise to the metal–metal cluster bonding configuration $|...3b_{2g}^2 6a_{1g}^2 5a_{2u}^2 8e_u^4 6e_g^2\rangle$, and the relative orbital energetics in this metal–metal bonding manifold are shown in Figure 7. Since the a_{2u} and e_g orbitals are π-bonding, the D_{4h}

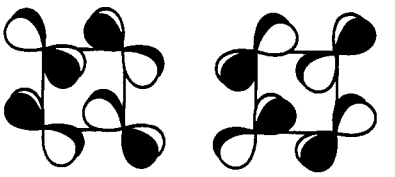

$6e_g$

III

$W_4(\mu\text{-}OH)_4(OH)_8$ cluster has four π electrons, and the doubly occupied e_g set represents a diradical. In this regard, the D_{4h} $W_4(\mu\text{-}OH)_4(OH)_8$ cluster may be considered as an inorganic analogue of cyclobutadiene, which has been both predicted[23-28] and shown experimentally[29-31] to be subject to Jahn–Teller distortions, resulting in a nonsquare equilibrium geometry.

For D_{4h} $W_4(\mu\text{-}OH)_4(OH)_8$, the electronic configuration of $|...e_g^2\rangle$ will give rise to the four possible states of symmetry A_{1g}, B_{1g}, B_{2g}, and A_{2g}. Since these states are nondegenerate, there can be no first-order Jahn–Teller effect.[32,33] However, a distortion that destroys D_{4h} symmetry can mix a nondegenerate ground state with excited states that have different symmetries in the undistorted cluster. This mixing can be treated by second-order perturbation theory and has been called a second-order Jahn–Teller effect.[34,35] The group-theoretical rule for the second-order Jahn–Teller effect is that the direct product of the irreducible representations of the two states must belong to the same representation as the vibrational mode that produces the distortion. Under D_{4h} symmetry we find that a b_{1g} distortion can mix A_{2g} and B_{2g} or A_{1g} and B_{1g} states. Similarly, a b_{2g} distortion can mix A_{1g} and B_{2g} or B_{1g} and A_{2g} states. These Jahn–Teller active vibrations are shown in IV, and both will distort the D_{4h} square

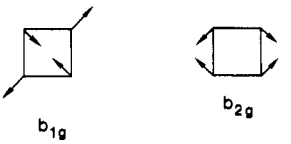

IV

cluster into D_{2h} symmetry. The b_{1g} mode will produce a rhomboidal distortion, and the b_{2g} mode will produce a rectangular distortion. It is important to emphasize that a priori we cannot predict which of the potentially active vibrational modes will give rise to distortion. This will depend on the energy gap between ground and nearby excited states, as well as the force constant. In the case of square cyclobutadiene, sophisticated electronic structure calculations predict the rectangular distortion to yield the lowest energy geometry.[27,28,36] In the case of square $W_4(\mu\text{-}OH)_4(OH)_8$, it is not possible for us to determine which distorted structure will have the lowest energy within the context of the

(23) Buenker, R. J.; Peyerimhoff, S. D. *J. Chem. Phys.* **1986**, *48*, 354.
(24) Dewar, M. J. S.; Kohn, M. C.; Trinajstic, N. *J. Am. Chem. Soc.* **1971**, *93*, 3437.
(25) Kollmar, H.; Stammler, V. J. *J. Am. Chem. Soc.* **1977**, *99*, 3583.
(26) Jafri, J. A.; Newton, M. J. *J. Am. Chem. Soc.* **1978**, *100*, 5012.
(27) Borden, W. T.; Davidson, E. R.; Hart, P. *J. Am. Chem. Soc.* **1978**, *100*, 388.
(28) Borden, W. T.; Davidson, E. R. *Acc. Chem. Res.* **1981**, *14*, 69.
(29) Masamune, S.; Sonto-Bachiller, F. A.; Machinguchi, T.; Bertie, J. E. *J. Am. Chem. Soc.* **1978**, *100*, 4889.
(30) Whitman, D. W.; Carpenter, B. K. *J. Am. Chem. Soc.* **1980**, *102*, 4272.
(31) Balley, T.; Masamune, S. *Tetrahedron* **1980**, *36*, 343.
(32) Jahn, H. A.; Teller, E. *Proc. R. Soc. London, A* **1937**, *16*, 220.
(33) Many examples of the Jahn–Teller theorem have been discussed in the literature. Two very good books include: (a) Engleman, R. *The Jahn–Teller Effect in Molecules and Crystals*; Wiley-Interscience: New York, 1972. (b) Bersuker, I. B. *The Jahn–Teller Effect and Vibronic Interactions in Modern Chemistry*; Plenum: New York, 1984. (c) For an excellent discussion, see: Pearson, R. G. *Proc. Natl. Acad. Sci. U.S.A.* **1975**, *72*, 2104.
(34) Pearson, R. G. *J. Am. Chem. Soc.* **1969**, *91*, 4947.
(35) Pearson, R. G. *J. Mol. Struct.* **1983**, *103*, 25.
(36) For an excellent discussion and summary of the cyclobutadiene radical cation and neutral molecule, see: Davidson, E. R.; Borden, W. T. *J. Chem. Phys.* **1983**, *87*, 4783.

Fenske–Hall formalism. However, we can use the Fenske–Hall method as a tool toward rationalizing the rhomboidal geometry of $W_4(\mu\text{-}OH)_4(OH)_8$ as a result of a second-order Jahn–Teller instability in the more symmetrical D_{4h} square structure.

From the above discussion it is clear that a distortion of the symmetrical D_{4h} cluster into D_{2h} symmetry is a feasible process based on considerations of the Jahn–Teller theorem. From group-theoretical considerations, it is expected that when the symmetry is lowered from D_{4h} to D_{2h}, the degeneracy of the e orbitals will be lifted. We have performed a calculation on $W_4(\mu\text{-}OH)_4(OH)_8$ in an idealized D_{2h} rhomboidal geometry and used group-theoretical considerations to map out a 1:1 correspondence between molecular orbitals of the D_{4h} and D_{2h} $W_4(\mu\text{-}OH)_4(OH)_8$ clusters.

A correlation diagram displaying these results is shown in Figure 8. Solid lines trace nondegenerate orbitals from D_{4h} to D_{2h} symmetry, and dashed lines connect degenerate orbitals in D_{4h} symmetry to their two nondegenerate counterparts in D_{2h} symmetry.

The six occupied molecular orbitals of the D_{2h} model $W_4(\mu\text{-}OH)_4(OH)_8$ cluster that are primarily involved in metal–metal cluster bonding are illustrated qualitatively in V. The 12 electrons

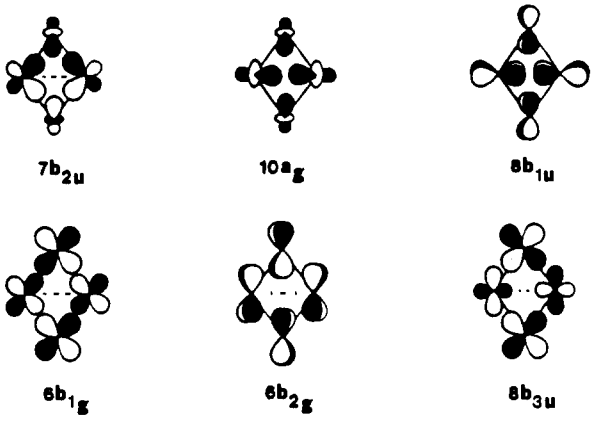

V

expected for tungsten will give rise to the metal–metal bonding configuration of $|...7b_{2u}^2 10a_g^2 8b_{1u}^2 6b_{1g}^2 6b_{2g}^2 8b_{3u}^2\rangle$, and the relative orbital energetics of the orbitals in this metal–metal bonding manifold are shown in Figure 8. Although all of these orbitals are metal–metal bonding, the nature of the bonding varies considerably. For example, the $6b_{1g}$ orbital is bonding between the wingtip and backbone atoms with the bonds concentrated along the four edges of the rhombus. The $8b_{3u}$ orbital is also concentrated along the four edges but is weakly antibonding between backbone atoms. Both the $7b_{2u}$ and $10a_g$ orbitals are delocalized across the faces as well as the edges of the triangles formed by the backbone and wingtip atoms. By contrast, both the $8b_{1u}$ and $6b_{2g}$ orbitals are delocalized π-bonding orbitals with respect to the W_4 plane. Thus overall, the symmetric D_{2h} rhomboidal $W_4(\mu\text{-}OH)_4(OH)_8$ cluster retains the eight σ and four π electrons and hence the analogy with cyclobutadiene.

Most important to our understanding of the bonding in the actual $W_4(\mu\text{-O-}i\text{-Pr})_4(\text{O-}i\text{-Pr})_8$ cluster is that distortion into a D_{2h} rhomboidal geometry yields two inequivalent pairs of tungsten atoms: wingtip and backbone. This introduces a bonding interaction between backbone atoms as seen for the $10a_g$ and $8b_{1u}$ orbitals shown in V. Furthermore, this inequivalence of wingtip and backbone tungsten atoms gives us our first clue toward understanding the asymmetric nature of the W–O bridges in the $W_4(\mu\text{-O-}i\text{-Pr})_4(\text{O-}i\text{-Pr})_8$ cluster.

The inequivalence of wingtip and backbone tungsten atoms in the rhomboidal geometry gives rise to a situation where the wingtip atoms are involved in stronger overall σ *and* π interactions with the bridging ligands than the backbone atoms. The magnitudes of these σ and π interactions are reflected in the W–μ-O overlap

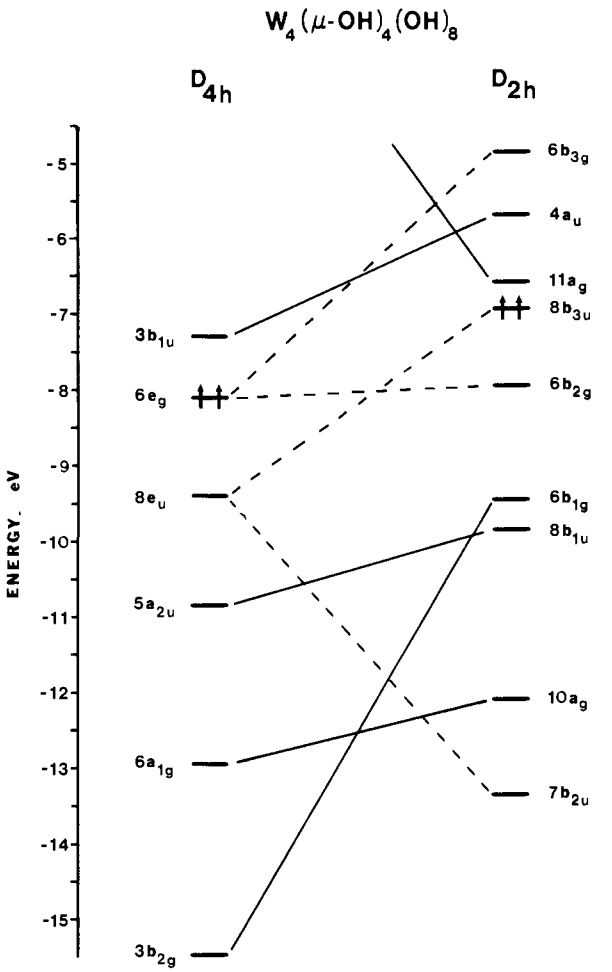

Figure 8. Correlation diagram comparing the relative orbital energies of $W_4(\mu\text{-}OH)_4(OH)_8$ in D_{4h} symmetry (left) and in the symmetrical rhomboidal D_{2h} geometry (right). Solid lines trace nondegenerate orbitals from D_{4h} to D_{2h} symmetry, while dashed lines connect degenerate orbitals in D_{4h} symmetry to their nondegenerate counterparts in D_{2h}.

Table VII. W–μ-O Overlap Populations

	W_b[a]	W_w[b]
O p_x–W d	0.052	0.106
O p_y–W d	0.002	0.062
O p_z–W d	0.024	0.036
totals	0.078	0.204

[a] Backbone. [b] Wingtip.

populations listed in Table VII for the D_{2h} $W_4(\mu\text{-}OH)_4(OH)_8$ cluster. The largest overlap populations involving W d orbitals occur between the oxygen p and wingtip tungsten d orbitals in the symmetrical geometry. The net result is that the total O p–W d overlap population is on the order of 50% larger for the wingtip relative to backbone tungsten atoms. Although the overlap populations can only be taken as an approximate measure of bond strength, the large differences in values between backbone and wingtip tungsten atoms attest to the importance of the interaction between wingtip tungsten atoms and bridging oxygen atoms.

Perhaps the most important observation of all is that the HOMO–LUMO gap is quite small. The Fenske–Hall method calculates this separation to be approximately 0.4 eV. This is an indication of a potential further second-order Jahn–Teller instability in the symmetric D_{2h} structure. As in the D_{4h} cluster, a vibronic motion that destroys D_{2h} symmetry can mix a nondegenerate ground state with low-lying excited states that have different symmetries in the undistorted cluster. In terms of molecular orbitals this becomes an interaction between a high-energy occupied MO and a low-energy unoccupied MO. Oftentimes this involves interaction of the HOMO and LUMO, as

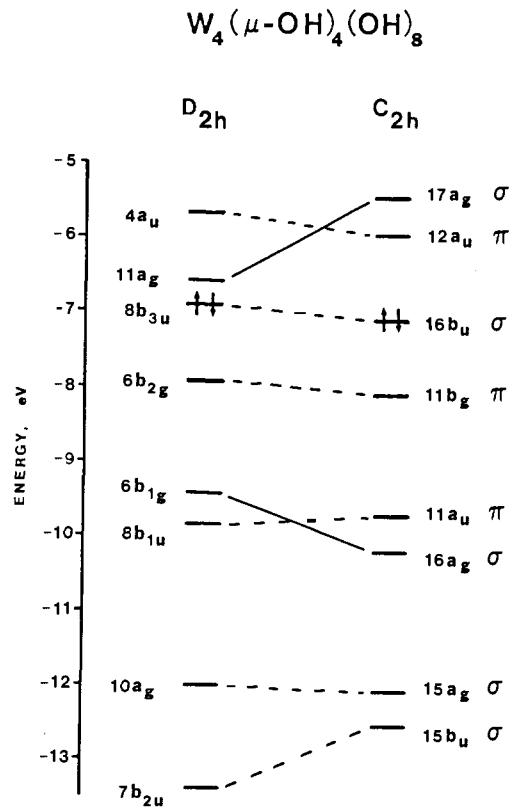

Figure 9. Correlation diagram comparing the relative orbital energies of $W_4(\mu\text{-}OH)_4(OH)_8$ in D_{2h} (left) and C_{2h} geometries (right). Solid lines trace those orbitals involved in second-order mixing from higher to lower symmetry, and dashed lines connect the remaining orbitals. The HOMO in each geometry is denoted by arrows.

in the D_{4h} case, or as demonstrated by Cotton and Fang[21] in their studies of a somewhat related metal atom cluster compound $W_4(OEt)_{16}$. However, this is by no means a prerequisite for a second-order effect.[35]

It is important to reemphasize that a priori we cannot unequivocally predict which of the potentially active D_{2h} vibrational modes will give rise to distortion. This will depend on the energy gap between ground and nearby excited states, as well as the force constant. However, we may use a Fenske–Hall calculation as a means to examine and rationalize the experimentally observed distortion. Examination of the D_{2h} character table reveals the presence of a Jahn–Teller active b_{1g} vibrational mode, which will produce the experimentally observed distortion. This vibrational mode is shown in VI and will shorten two opposing edges of an M_4 rhombus.

VI

This b_{1g} vibrational mode is expected to mix the $6b_{1g}$ and $11a_g$ molecular orbitals of D_{2h} $W_4(\mu\text{-}OH)_4(OH)_8$ since their direct product is b_{1g}, the same as the vibrational mode in consideration. Accordingly, calculations were performed on a distorted $W_4(\mu\text{-}OH)_4(OH)_8$ cluster in C_{2h} symmetry with idealized bond lengths and angles from the X-ray structure of $W_4(O\text{-}i\text{-}Pr)_{12}$. The results of the C_{2h} calculations are compared to the D_{2h} results in the form of a correlation diagram shown in Figure 9. The results of this correlation diagram clearly show that the b_{1g} distortion mixes the $6b_{1g}$ and $11a_g$ orbitals of the D_{2h} cluster in that the former is lowered and the latter raised in energy upon distortion to C_{2h} symmetry. As expected, both orbitals now have a_g symmetry in the new point group, and the magnitude of the HOMO–LUMO gap has increased considerably as a result of distortion. Since the orbitals involved in the mixing are primarily metal–metal

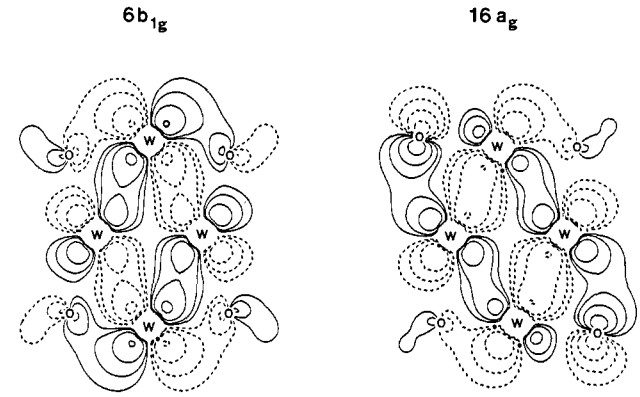

Figure 10. Contour plots illustrating the effect of Jahn–Teller distortion on the occupied $6b_{1g}$ orbital of D_{2h} $W_4(\mu\text{-}OH)_4(OH)_8$ (left) as it transfers into the $16a_g$ orbital in C_{2h} symmetry (right). This plot is taken in the W_4 plane and contains the four W atoms and four oxygen atoms of the bridging OH ligands. Positive and negative contour values are indicated by solid and dashed lines, respectively. Contour values for this and all subsequent plots begin at ± 0.02 e/Å^3 and increase by a factor of 2 at each step.

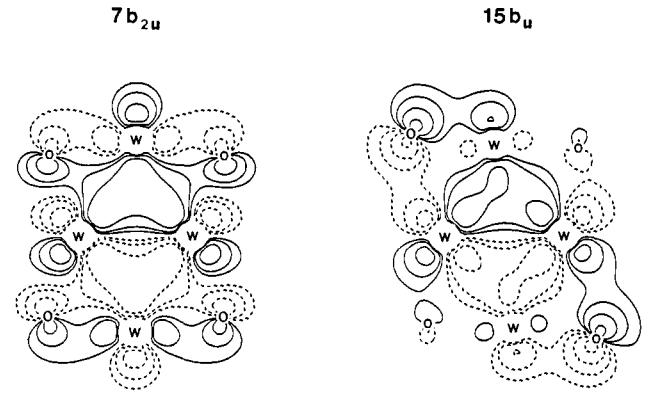

Figure 11. Contour plots illustrating the effect of Jahn–Teller distortion on the occupied $7b_{2u}$ orbital of D_{2h} $W_4(\mu\text{-}OH)_4(OH)_8$ (left) as it transfers into the $15b_u$ orbital in C_{2h} symmetry (right).

bonding in character, it is easy to see why the distortion manifests itself primarily as a change in the various metal–metal distances. Now we can return to our original question of how the distortion affects our view of the metal–metal and metal–ligand bonding within the $W_4(\mu\text{-}OH)_4(OH)_8$ cluster. The answer, which is indicated by the calculated results, is that this distortion induces a localization in the metal–metal bonding of the cluster framework.

To better illustrate this change induced in the metal–metal bonding picture, we can follow the localization phenomenon with the aid of selected contour plots of pertinent orbitals in D_{2h} and C_{2h} symmetry. First and foremost, the changes observed upon energy lowering in the $6b_{1g}$ orbital (D_{2h}) as it transfers into the $16a_g$ orbital (C_{2h}) is shown with the aid of contour plots in Figure 10. These and all subsequent plots are displayed as a slice containing the $W_4(\mu\text{-}O)_4$ plane before (D_{2h}) and after (C_{2h}) distortion. The localization of metal–metal bonding in two opposing edges of the rhombus is readily apparent in the plots. Figure 11 follows the transfer of the $7b_{2u}$ orbital (D_{2h}) into the $15b_u$ orbital (C_{2h}) upon distortion. Again, the localization induced in opposing W–W bonds shows up nicely in these plots. This same localization phenomenon is observed in the W_4 π system as well, and Figure 12 compares the bonding in the $6b_{2g}$ orbital (D_{2h}) as it transfers into $11b_g$ orbital (C_{2h}) of the distorted rhombus.

The most important point regarding the asymmetric nature of the W–O bridges is that the distortion allows for better overlap, and hence better interaction, between edge-bridging ligands and the wingtip tungsten atoms. It is important to emphasize here that this concept of a stronger interaction between wingtip atoms and edge-bridging ligands is by no means a new one. Harris and Bradley[37] noted, for example, that a butterfly arrangement of Fe

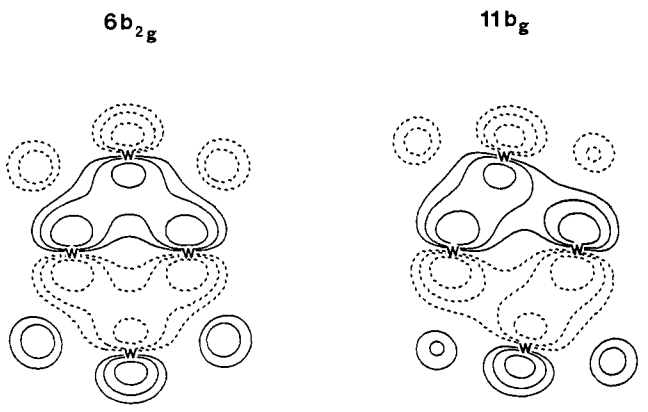

Figure 12. Contour plots illustrating the effect of Jahn–Teller distortion on the occupied $6b_{2g}$ orbital of D_{2h} $W_4(\mu\text{-}OH)_4(OH)_8$ (left) as it transfers into the $11b_g$ orbital in C_{2h} symmetry (right). These plots are taken in a plane 0.25 Å above the W_4 plane.

atoms in $Fe_4C(CO)_{12}^{2-}$ resulted in a stronger interaction between wingtip Fe atoms and carbido carbon p orbitals than backbone Fe atoms as judged by Fe–C overlap population. This difference in bonding between Fe and C is reflected in Fe–C distances, which are notably shorter for wingtip than backbone Fe atoms, a situation not at all unlike that observed in $W_4(\mu\text{-}OH)_4(OH)_8$ with respect to the μ-OR ligands.

NMR Studies. The fluxional behavior of the $W_4(O\text{-}i\text{-}Pr)_{12}$ molecule and the thermodynamic and activation parameters associated with the equilibrium between $W_4(O\text{-}i\text{-}Pr)_{12}$ and $W_2(O\text{-}i\text{-}Pr)_6$ (eq 1) have been determined by detailed NMR studies. These are discussed in detail in a following paper. It is sufficient to note here that the equilibrium between the two is chemically very slow below 0 °C and consequently the NMR spectra of the individual compounds can be recorded. The ^1H NMR spectrum of $W_2(O\text{-}i\text{-}Pr)_6$ is, as expected, simple, consisting of a single methyne septet and methyl doublet analogous to that of $Mo_2(O\text{-}i\text{-}Pr)_6$.

The ^1H NMR spectrum of $W_4(O\text{-}i\text{-}Pr)_{12}$ at −40 °C is shown in Figure 13 in the methyne region. There are five methyne septets, four of equal intensity and one twice as intense. While there are six crystallographically different O-*i*-Pr ligands, the two terminal O-*i*-Pr ligands on the backbone tungsten atoms differ little with respect to their orientation to the cluster. It is, therefore, not unreasonable to assign the methyne resonance of intensity 2 to the backbone O-*i*-Pr ligands. The two crystallographically independent bridging O-*i*-Pr ligands are very notably different in the solid-state molecular structure, as are the terminal O-*i*-Pr ligands bonded to the wingtip tungsten atoms. The latter have their methyne protons directed either proximal or distal to the W_4 core. Thus, assuming the methyl protons of the O-*i*-Pr ligands attached to the backbone tungsten atoms are isochronous, the spectrum shown in Figure 13 is consistent with the presence of an analogous structure to that in the solid state. We have previously demonstrated that this species remains tetranuclear in solution by cryoscopic molecular weight measurements.

Concluding Remarks. This work provides the first structural characterization of both an unligated $W_2(OR)_6$ compound and a 12-electron $M_4(OR)_{12}$ cluster. It also provides the first example of the preparation and characterization of a dinuclear M–M multiple-bonded compound and its dimer, the corresponding M_4 cluster. As noted in the introduction, previous workers have shown that M–M quadruple bonds may be coupled by condensation reactions.[10,11] Here the elimination of a labile ligand, MeOH, is irreversible as is our coupling of $(Mo{\equiv}Mo)^{6+}$ units by halide for alkoxide exchange reactions.[4,5] Given the sizable activation energy for their interconversion, this will allow for studies of their individual reactivity toward substrates of interest.

The Fenske–Hall MO calculations have demonstrated an analogy between the 12-electron M_4 cluster and cyclobutadiene.

(37) Harris, S.; Bradley, J. S. *Organometallics* **1984**, *3*, 764.

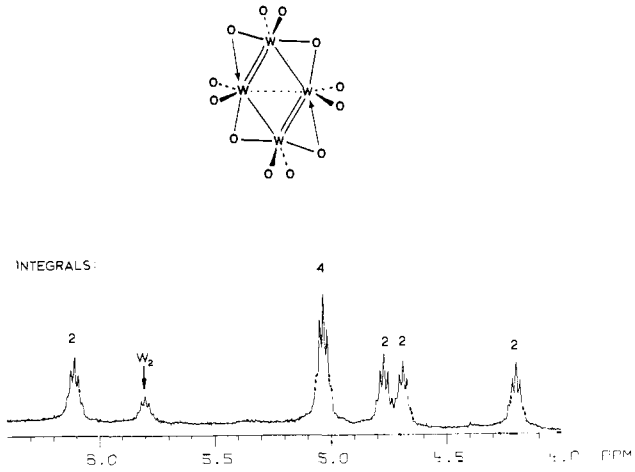

Figure 13. 360-MHz ^1H NMR spectrum of $W_4(O\text{-}i\text{-}Pr)_{12}$ in toluene-d_8 solution at −40 °C. Only the methyne region of the spectrum is shown. The signal at δ 5.8, marked with an arrow, arises from $W_2(O\text{-}i\text{-}Pr)_6$.

The distortion from a D_{4h} structure is apparently derived from a second-order Jahn–Teller distortion in parallel to C_4H_4. A further analogy between C_4H_4 and $W_4(O\text{-}i\text{-}Pr)_{12}$ is developed in a companion paper. Though the calculations presented here cannot determine why the observed structure is preferred to others such as those found for $Mo_4Cl_4(\mu\text{-}O\text{-}i\text{-}Pr)_8$ or $Mo_4Br_4(\mu_3\text{-}O\text{-}i\text{-}Pr)_2(\mu\text{-}O\text{-}i\text{-}Pr)_4(O\text{-}i\text{-}Pr)_2$, it is pleasing to note that the observed structure is based on MO_4 fragments, which avoid the use of radial M–O bonds. In this regard, we see that the $W_4(O\text{-}i\text{-}Pr)_{12}$ structure is preferred to the D_{4h} $Mo_4Cl_4(O\text{-}i\text{-}Pr)_8$ structure. This can be understood in terms of the *radial cluster influence*[22] of the ligands, which follows the order RO > halide. It is also interesting to note that, while the square and butterfly $Mo_4X_4(O\text{-}i\text{-}Pr)_8$ structures (X = Cl and Br, respectively) represent fragments of the cube-octahedron $M_6(\mu_3\text{-}X)_8$ unit, the present $M_4(O)_{12}$ unit represents a distorted fragment of the $M_6(\mu_2\text{-}X)_{12}$ unit commonly found for early-transition-metal halide clusters, e.g. M = Nb, Ta, Mo, W.[11]

Experimental and Computational Procedures

Physical Techniques. ^1H NMR spectra were recorded on a Nicolet NT-360 spectrometer at 360 MHz in dry and oxygen-free toluene-d_8 or benzene-d_6. All ^1H NMR chemical shifts are reported (ppm) relative to the CHD_2 quintet of toluene-d_8 (set at δ 2.09) or the ^1H impurity in benzene-d_6 (set at δ 7.15). Infrared spectra were recorded on a Perkin-Elmer 283 spectrophotometer as Nujol mulls between CsI plates.

Synthesis. All reactions were carried out under an atmosphere of dry and oxygen-free nitrogen using standard Schlenk and glovebox techniques. Hexane and toluene were degassed and eluted from an activated copper catalyst and molecular sieve columns and then stored over sieves and under nitrogen. Diethyl ether, 1,2-dimethoxyethane, and THF were distilled from sodium benzophenone and stored under nitrogen and over sieves. $W_2(O\text{-}t\text{-}Bu)_6$ was prepared following literature procedures.[7] Elemental analyses were performed by Alfred Bernhardt Microanalytishes Laboratorium, West Germany.

$W_4(O\text{-}i\text{-}Pr)_{12}$. $W_2(O\text{-}t\text{-}Bu)_6$ (1.000 g, 1.24 mmol) was dissolved in hexane (8 mL) and the solution cooled to 0 °C. 2-Propanol (5 mL) was added, and the solution changed color from deep red to pale yellow, initially, becoming gradually darker. After 4 h, the solvent was removed from the black solution in vacuo, and the black solid was redissolved in the minimum amount of pentane (ca. 4 mL) at room temperature. The solution was kept at −15 °C for 15 h whereupon a large amount of black crystals (0.534 g) had formed. The solution was filtered, the volume of solvent reduced by about half, and the flask replaced at −15 °C. After 15 h, another crop of black crystals was isolated. The solids were combined to give total yield of 0.730 g (0.51 mmol), 81.5% based on **2**.

Anal. Calcd for $WO_3C_9H_{21}$: C, 29.92; H, 5.82. Found: C, 29.78; H, 5.78. MS: base peak at *m/e* 722 attributable to $[W_2(O\text{-}i\text{-}Pr)_6]^+$.

^1H NMR in benzene-d_6 solution at 360 MHz and 22 °C: δ-($OCHMe_2$) = 6.1 (br), 5.0 (sharp), 4.7 (br), 4.2 (br) of relative intensity 1:2:2:1, respectively; $\delta(OCHMe_2)$ = 1.2–1.6 (br, overlapping resonances).

IR spectrum (Nujol mull, CsI plates): 1340 w, 1320 m, 1260 m, 1160 m, 1107 s, 980 s, 945 w, 935 w, 845 m, 830 m, 800 m, 602 m, 590 m, 455 w cm^{-1}.

Alternate Synthesis. $W_2(O\text{-}t\text{-}Bu)_6$ (0.500 g, 0.62 mmol) was taken up in a minimum amount of pentane (30 mL) and cooled to 0 °C. A large

excess of *i*-PrOH (ca. 5–10 mL) was added to the stirred solution via cannula transfer. The color of solution changed from red to brown. The reaction was allowed to warm to room temperature after 3 h, and the reaction solvents were removed in vacuo. The solids were redissolved in hexane and cooled to −15 °C. After 1 day, many large black crystals were present. These crystals were obtained by filtration to give approximately a 60% yield (based on W) of the pure $W_4(O\text{-}i\text{-}Pr)_{12}$ compound (by ^1H NMR).

$W_4(O\text{-}i\text{-}Pr)_{12}$:$W_2(O\text{-}i\text{-}Pr)_6$. $W_2(O\text{-}t\text{-}Bu)_6$ (0.500 g, 0.62 mmol) was taken up in a minimum amount of 1,2-dimethoxyethane (40 mL) and cooled to 0 °C ($W_2(O\text{-}t\text{-}Bu)_6$ is not very soluble in dme). A large excess of *i*-PrOH (ca. 5–10 mL) was added to the stirred solution via cannula transfer. The color of solution changed very slowly from red to brown. The solution was stirred at 0 °C for several hours, the volume was reduced by half, and the solution was cooled to −15 °C. After 1 day, many small black crystals were present and were mixed with a small amount of yellow crystals. The crystals were collected by filtration and dried in vacuo to give approximately a 60% yield based on W. This procedure yields black crystals $W_2(O\text{-}i\text{-}Pr)_6$:$W_4(O\text{-}i\text{-}Pr)_{12}$ based on the X-ray study.

Preparation of $W_2(O\text{-}i\text{-}Pr)_6$ via $W_2(O\text{-}i\text{-}Pr)_6(NMe_3)_2$. From $W_2(O\text{-}t\text{-}Bu)_6$. $W_2(O\text{-}t\text{-}Bu)_6$ (397 mg, 0.49 mmol) was placed in a 50-mL Schlenk flask, and 15 mmol of NMe_3 was condensed under vacuum at −196 °C. The solution was warmed to 0 °C (*Caution*! NMe_3 boils at +5 °C), and nitrogen was admitted. On addition of 1.5 mL of 2-propanol, the solution changed color from deep red to brown-yellow and was stirred at 0 °C for 1 h. The volatile components were removed under vacuum as rapidly as possible at room temperature to leave a pale brown-yellow residue, which after being pumped under a dynamic vacuum at room temperature for about 1 h, turned pale yellow. ^1H and ^{13}C NMR spectra of this yellow product showed it to be spectroscopically pure $W_2(O\text{-}i\text{-}Pr)_6$, obtained in quantitative yield.

^1H NMR in toluene-d_8 at 23 °C: $\delta(OCHMe_2)$ = 5.67 (sept) $^3J_{H-H}$ = 6 Hz; $\delta(OCHMe_2)$ = 1.49 (d).

^{13}C NMR in toluene-d_8 at −13 °C: $\delta(OCHMe_2)$ = 83.0.

From $W_2(NMe_2)_6$. $W_2(NMe_2)_6$ (1.00 g, 1.58 mmol) was partially dissolved in hexane (10 mL), and 2-propanol (5 mL) was added. The pale yellow solution turned deep green, and after being stirred at room temperature for 0.5 h, the solution was cooled to liquid-nitrogen temperature and the flask evacuated. NMe_3 (20 mmol) was condensed in from a calibrated vacuum manifold, the solution was warmed to 0 °C, and nitrogen was admitted to the flask. After the mixture was stirred for 4 h at 0 °C, the volatile components were removed at room temperature to give a golden yellow-brown residue, which on continued pumping turned pale yellow. The solid obtained was shown to be spectroscopically pure $W_2(O\text{-}i\text{-}Pr)_6$ (0.92 g, 1.27 mmol) by ^1H NMR spectroscopy, with an isolated yield of 80%.

Attempted Direct Preparation from $W_2(O\text{-}t\text{-}Bu)_6$ at 50 °C. $W_2(O\text{-}t\text{-}Bu)_6$ (0.23 g, 0.29 mmol) was placed in a 30-mL Schlenk flask, and 2-propanol (15 mL) was added. The flask was placed in an oil bath at +50 °C, and the deep red solution rapidly became pale yellow. After 5 min, a small aliquot was taken, the solvent was removed, and the sample was redissolved in C_6D_6. ^1H NMR spectroscopy indicated the presence of many different types of methine protons as well as *tert*-butyl resonances. The mixture was stirred for a total of 2 h, and then the solvent was removed in vacuo to give a dark brown solid. ^1H NMR spectroscopy showed this to be mainly $W_2(O\text{-}i\text{-}Pr)_6$, together with $W_4(O\text{-}i\text{-}Pr)_{12}$ and some decomposition products.

Crystallographic Studies. General operating procedures and listings of programs have been previously reported.[38] A suitable small crystal fragment was selected by inert-atmosphere handling techniques. The crystal was transferred to the goniostat where it was cooled to −156 °C for characterization and data collection. A summary of crystal data is given in Table VIII.

A systematic search of a limited hemisphere of reciprocal space yielded a set of reflections that exhibited no symmetry or systematic extinctions. The reflections were indexed with a triclinic lattice, and the space group $P\bar{1}$ was confirmed by the successful solution and refinement of the structure.

A total of 7316 reflections was collected, corrected for L–P factors, and averaged to a unique set of 4935. The data were corrected for absorption (see Table VIII). The R for the averaging was 0.052 for 2263 reflections, measured more than once. The structure was solved by the usual combination of direct methods (MULTAN78) and Fourier techniques. The asymmetric unit contained two halves of two different centrosymmetric complexes. The one compound is tetranuclear, with a planar W_4 moiety (a flattened butterfly), and the other molecule is dinuclear, with a W–W triple bond. The tetranuclear compound is numbered W(1) through C(26), and the dinuclear compound, W(27) through C(39). In spite of the low-temperature data, the thermal parameters are quite large. In particular, O(23), which is associated with the "semibridging" O-*i*-Pr ligand, shows motion in the W_4 plane. No hydrogen atoms were located, but all were introduced in fixed calculated positions. The full-matrix least-squares refinement was completed with anisotropic thermal parameters on all non-hydrogen atoms.

Table VIII. Summary of Crystal Data for the $W_4(O\text{-}i\text{-}Pr)_{12}$:$W_2(O\text{-}i\text{-}Pr)_6$ Molecule

empirical formula	$W_4O_{12}C_{36}H_{84}$:$W_2O_6C_{18}H_{42}$
color of crystal	black
cryst dimens, mm	0.16 × 0.12 × 0.08
space group	$P\bar{1}$
cell dimens	
temp, °C	−156
a, Å	12.277 (3)
b, Å	12.890 (3)
c, Å	12.118 (3)
α, deg	94.60 (1)
β, deg	81.86 (1)
γ, deg	83.92 (1)
Z (molecules/cell)	1
V, Å^3	1878.99
d_{calcd}, g/cm^3	1.915
wavelength (λ), nm	0.71069
mol wt	1083.34
linear abs coeff, cm^{-1}	93.994
detector to sample dist, cm	22.5
sample to source dist, cm	23.5
av ω scan width at half-height	0.25
scan speed, deg/min	4.0
scan width, deg + dispersion	1.8
individual bkgd, s	8
aperture size, mm	3.0 × 4.0
2θ range, deg	6–45
total no. of reflcns collected	7316
no. of unique intens	4935
no. of $F > 0.0$	4481
no. with $F > 3.0\sigma(F)$	4042
$R(F)$	0.0746
$R_w(F)$	0.0691
goodness of fit for last cycle	1.671
max δ/σ for last cycle	0.05

The final difference map contained several peaks of ca. 3 e/Å^3; all of these were in the immediate vicinity of the W atoms. Otherwise the map was featureless. The large residuals may be caused by the overall large thermal vibrations or by an incomplete absorption correction.

Calculational Details. The coordinates for the model compound of formula $W_4(OH)_{12}$ were idealized to C_{2h} point symmetry, but otherwise bond lengths and angles were taken from the crystal structure of $W_4(O\text{-}i\text{-}Pr)_{12}$ reported here. The W–W distances used were 2.502, 2.732, and 2.807 Å for the "short", "long", and "backbone" W–W distances, respectively. The terminal W–O distances were set at the average value of 1.891 Å to maintain C_{2h} symmetry. The O–H distances were assumed to be 0.96 Å.

The coordinates for the D_{2h} $W_4(OH)_{12}$ cluster were idealized with five W–W distances placed at 2.655 Å, the average of those used in the C_{2h} model. The tungsten to μ-O and terminal O distances used were 2.100 and 1.920 Å, respectively. The O–H distance was assumed to be 0.96 Å, and the terminal W–O–H angles were fixed at 140°. In the D_{4h} square $W_4(\mu\text{-}OH)_4(OH)_8$ molecule, a W–W distance of 2.40 Å was selected for the four equivalent edges. The W–O distances and W–O–H angles were as noted above.

Molecular orbital calculations were performed by the method of Fenske and Hall, which has been described in detail elsewhere.[18] The Fenske–Hall method is an approximate Hartree–Fock Roothaan SCF-LCAO procedure, and the final results depend only upon the chosen atomic basis set and internuclear distances. All calculations reported here were obtained at the Indiana University Computational Chemistry Center with a VAX 11/780 computer system. Contour plots were generated on a Talaris 800 laser printer, with solid lines representing positive density contours and dashed lines representing negative density contours.

All atomic wave functions were generated by a best fit to Herman–Skillman atomic calculations by the method of Bursten, Jensen, and Fenske.[39] Contracted double-ζ representations were used for the W 5d

(38) Chisholm, M. H.; Folting, K.; Huffman, J. C.; Kirkpatrick, C. C. *Inorg. Chem.* **1984**, *23*, 1021.

(39) Bursten, B. E.; Jensen, J. R.; Fenske, R. F. *J. Chem. Phys.* **1978**, *68*, 3320.

and O 2p AO's. Basis functions for the W atom were derived for a +1 oxidation state with the 6s and 6p exponents fixed at 1.8.[40] An exponent of 1.16 was used for the H 1s atomic orbital.[41]

Acknowledgment. We thank the National Science Foundation and the Wrubel Computing Center for support. We thank Professor E. R. Davidson of Indiana University for helpful discussions. D.L.C. was the 1985/1986 Indiana University General Electric Fellow. The VAX 11/780 is an NSF-supported departmental facility, Grants CHE-83-09446 and CHE-89-05851.

(40) Tungsten basis functions were as previously described: Blower, P. J.; Chisholm, M. H.; Clark, D. L.; Eichhorn, B. W. *Organometallics* **1986**, *5*, 2125.
(41) Hehre, W. J.; Steward, R. F.; Pople, J. A. *J. Chem. Phys.* **1969**, *51*, 2657.

Registry No. $W_4(O\text{-}i\text{-}Pr)_{12}$, 104911-26-4; $W_2(O\text{-}t\text{-}Bu)_6$, 57125-20-9; $W_2(O\text{-}i\text{-}Pr)_6$, 71391-16-7; $W_2(NMe_2)_6$, 54935-70-5; $W_4(\mu\text{-}OH)_4(OH)_8$, 110825-38-2; W, 7440-33-7.

Supplementary Material Available: Tables of anisotropic thermal parameters, bond distances, and bond angles (4 pages); listing of F_o and F_c values (11 pages). Ordering information is given on any current masthead page.

Studies of Hypervalent Iron in Aqueous Solutions. 1. Radiation-Induced Reduction of Iron(VI) to Iron(V) by CO_2^-

Benon H. J. Bielski* and M. J. Thomas†

Contribution from the Department of Chemistry, Brookhaven National Laboratory, Upton, New York 11973. *Received April 20, 1987*

Abstract: Iron(VI) can be reduced in aqueous solutions to iron(V) by pulse radiolytically generated CO_2^-, $k_3 = (3.5 \pm 0.1) \times 10^8$ M^{-1} s^{-1}. The respective UV and visible spectra for these hypervalent oxidation states of iron are reported. It was found that formate reacts 10^5 times faster with Fe(V) than with Fe(VI). Other kinetic rate measurements include the following: $k_4[O_2^- + Fe(VI)] = (5.71 \pm 0.17) \times 10^3$, k[NADH + Fe(VI)] = 77.1 ± 4.4, k[HCOONa + Fe(VI)] = (2.33 ± 0.4) × 10^{-2}, k[EtOH + Fe(VI)] = (1.47 ± 0.7) × 10^{-3}, k[DTPA + Fe(VI)] = (8.53 ± 0.32) × 10^{-4}, k[HCOONa + Fe(V)] = (2.48 ± 0.32) × 10^3 M^{-1} s^{-1}. The results are discussed in terms of their possible role in Fe(VI) oxidation processes.

Despite considerable evidence for the involvement of Fe(IV)/Fe(V) in iron-catalyzed oxidation/hydroxylation processes, little tangible information has been forthcoming concerning these oxidation states in the field of aqueous inorganic chemistry.[1-12] While the chemistry of Fe(VI) in aqueous solutions is well reviewed,[13,14] similar information on Fe(V) is, with exception of a short report from this laboratory,[15] scant and limited to research reports on high-temperature melts and the solid state.

Iron ferrates (K_2FeO_4, $BaFeO_4$, etc.) are easily prepared in relatively pure form.[16,17] They are very stable, safe, and strong oxidizing agents. In several reactions they were shown to display a high degree of selectivity.[2-4,6-8,11,18] In aqueous solutions Fe(VI) is present as the FeO_4^{2-} ion, believed to have a tetrahedral structure similar to its geometry in the solid state.[19,20] The four oxygens in the molecule were shown to be equilvalent and apparently exchange in water slowly.[20] While aqueous FeO_4^{2-} solutions are relatively stable in the pH range between 9 and 10.5, they deteriorate rapidly in more acidic media with evolution of oxygen. The decomposition process is accelerated by ferric oxides/hydroxides, which accumulate and precipitate as the reaction progresses. In basic media FeO_4^{2-} apparently decomposes by a complex disproportionation mechanism.[13,21-23] Recent determinations of the pK's of FeO_4^{2-} (pK_1 = 3.5; pK_2 = 7.8) and its decomposition rates over a very broad pH range (2–9.5) have significantly advanced the understanding of the aqueous chemistry of Fe(VI).[13] $E°$'s have been estimated to be near −2.20 V in acid media and −0.72 V in alkaline solutions.[24]

Until recently, formation of Fe(V) had been observed only in high-temperature melts.[25-28] X-ray studies of isolated crystals from such melts suggest that the iron is present in the FeO_4^{3-} form.[26] Although there are claims that stable solutions of K_3FeO_4 were prepared in cold alkaline solutions by dissolving the salt isolated from melts,[29] pulse radiolytically generated FeO_4^{3-} in 5 N NaOH at ambient temperatures has a relatively short lifetime (k_{decay} = 4 s^{-1}).[15]

† Present address: Department of Biochemistry, Wake Forest University, Winston-Salem, NC 27103.

(1) Felton, R. H.; Owen, G. S.; Dolphin, D.; Fajer, J. *J. Am. Chem. Soc.* **1971**, *93*, 6332.
(2) Audette, R. J.; Quail, J. W.; Smith, P. J. *Tetrahedron Lett.* **1971**, 279.
(3) Audette, R. J.; Quail, J. W.; Smith, P. J. *J. Chem. Soc., Chem. Commun.* **1972**, 38.
(4) BeMiller, J. N.; Vithal, G. K.; Darling, S. D. *Tetrahedron Lett.* **1972**, 4143.
(5) Groves, J. T.; Van Der Puy, M. *J. Am. Chem. Soc.* **1974**, *96*, 5274.
(6) Williams, D. H.; Riley, J. T. *Inorg. Chim. Acta* **1974**, *8*, 177.
(7) Groves, J. T.; Swanson, W. W. *Tetrahedron Lett.* **1975**, 1953.
(8) Groves, J. T.; McClusky, G. A. *J. Am. Chem. Soc.* **1976**, *98*, 859.
(9) Groves, J. T.; Nemo, T. E.; Myers, R. S. *J. Am. Chem. Soc.* **1979**, *101*, 1032.
(10) Groves, J. T.; Haushalter, R. C.; Nakamura, M.; Nemo, R. E.; Evans, B. J. *J. Am. Chem. Soc.* **1981**, *103*, 2884.
(11) Groves, J. T.; Nemo, T. E. *J. Am. Chem. Soc.* **1983**, *105*, 6243.
(12) Bartzatt, R.; Tabatabai, A.; Carr, J. *Synth. React. Inorg. Met.-Org. Chem.* **1985**, *15*, 1171.
(13) Carr, J. D.; Kelter, P. B.; Tabatabai, A.; Spichal, D.; Erickson, J.; McLaughlin, C. W. Proceedings of the Conference on Water Chlorination and Chemical Environment Impact Health Effects, 1985.
(14) Levanson, W.; McAuliffe, C. A. *Coord. Chem. Rev.* **1974**, *12*, 151.
(15) Rush, J. D.; Bielski, B. H. J. *J. Am. Chem. Soc.* **1986**, *108*, 523.
(16) Thompson, G. W.; Ockerman, L. T.; Schreyer, J. M. *J. Am. Chem. Soc.* **1951**, *73*, 1379.
(17) Audette, R. J.; Quail, J. W. *Inorg. Chem.* **1972**, *11*, 1904.
(18) BeMiller, J. N.; Darling, S. D. U.S. Patent 3 632 802, 1972.
(19) Goff, H.; Murmann, R. K. *J. Am. Chem. Soc.* **1971**, *93*, 6058.
(20) Hoppe, M. L.; Schlemper, E. O.; Murmann, R. K. *Acta Crystallogr., Sect. B: Struct. Crystallogr. Cryst. Chem.* **1982**, *B38*, 2237.
(21) Ettel, F.; Veprek-Siska, J. *Collect. Czech. Chem. Commun.* **1969**, *34*, 2182.
(22) Ernst, T.; Wawrzenczyk, M.; Cyfert, M.; Wronska, M. *Bull. Acad. Pol. Sci., Ser. Sci. Chim.* **1979**, *27*, 773.
(23) Kalecinski, J. *Rocz. Chem.* **1967**, *41*, 661.
(24) Wood, R. H. *J. Am. Chem. Soc.* **1958**, *80*, 2038.
(25) Klemm, W.; Wahl, K. *Angew. Chem.* **1953**, *65*, 261; **1954**, *66*, 470.
(26) Scholder, v. R.; Bunsen, v. H.; Kindervater, F.; Zeiss, W. *Z. Anorg. Allg. Chem.* **1955**, *282*, 268.
(27) Wahl, K.; Klemm, W.; Wehrmeyer, G. *Angew. Chem., Int. Ed. Engl.* **1962**, *1*, 322.
(28) Temple, T. B.; Thickett, G. W. *Aust. J. Chem.* **1973**, *26*, 1137.

0002-7863/87/1509-7761$01.50/0